# Real-time monitoring of thermal processes by reduced order modeling

José V. Aguado[1], Antonio Huerta[2,3,*], Francisco Chinesta[1] and Elías Cueto[4]

[1] Institut de Recherche en Génie Civil et Mécanique (GeM UMR CNRS 6183),
Ecole Centrale de Nantes.
1 rue de la Noë, BP 92101, F-44321 Nantes cedex 3, France.
e-mail: {jose.aguado-lopez,francisco.chinesta}@ec-nantes.fr, web http://rom.ec-nantes.fr
[2]Laboratori de Calcul Numeric (LaCaN). Departament de Matematica Aplicada III
E.T.S. de Ingenieros de Caminos, Canales y Puertos,
Universitat Politecnica de Catalunya, BarcelonaTech, 08034 Barcelona, Spain.
e-mail: antonio.huerta@upc.edu, web http://www.lacan.upc.edu
[3]Zienkiewicz Centre for Computational Engineering, College of Engineering,
Swansea University, Swansea SA2 8PP, UK.
[4]Aragon Institute of Engineering Research (I3A),
Universidad de Zaragoza, Maria de Luna 3, E-50018 Zaragoza, Spain.
e-mail: ecueto@unizar.es, web http://amb.unizar.es

## SUMMARY

This work presents a simple technique for real-time monitoring of thermal processes. Real-time simulation-based control of thermal processes is a big challenge because high-fidelity numerical simulations are costly and cannot be used, in general, for real-time decision making. Very often, processes are monitored or controlled with a few measurements at some specific points. Thus, the strategy presented here is centered on fast evaluation of the response only where it is needed. To accomplish this, classical harmonic analysis is combined with recent model reduction techniques. This leads to an advanced harmonic methodology, which solves in real-time the transient heat equation at the monitored point.

In order to apply the *reciprocity principle*, harmonic analysis is used in the space-frequency domain. Then, Proper Generalized Decomposition, a reduced order approach, pre-computes a transfer function able to produce the output response for a given excitation. This transfer function is computed offline and only once. The response at the monitoring point can be recovered performing a computationally inexpensive post-processing step. This last step can be performed online for real-time monitoring of the thermal process. Examples show the applicability of this approach for a wide range of problems ranging from fast temperature evaluation to inverse problems.

## 1. INTRODUCTION

Many thermal manufacturing processes require monitoring temperature and, moreover, being able to determine from these measurements if the process is running as designed. Typically these measurements are provided by some sensors (e.g. thermocouples) strategically placed. Consider,

---

for instance, an industrial thermal process involving an external excitation, a heat source, moving on the surface of the considered part. This is typical of composite manufacturing processes. Today it is still a challenge to post-process these temperature measurements to monitor in real-time the correct evolution of the thermal process, or to control the heat source, or to identify defects, material properties or power oscillations, etc. This paper proposes a fast strategy to determine temperature at a desired monitoring point. More precisely, the approach presented here allows to compute in real-time temperature at a point of interest given an arbitrary transient heat source traveling along a Neumann or Robin boundary.

The strategy proposed revolves on the reciprocity principle [1] extensively used in mechanics, dynamics, electromagnetic or wave scattering problems. Note that, in general, this principle is not applicable for the heat equation because of the lack of symmetry introduced by the first time derivative. This paper proposes to adopt the reciprocity principle also to the heat equation. For this, the heat equation is recast in the frequency domain. Details and proofs on this novel approach are presented here.

Another novelty is to apply the Proper Generalized Decomposition method (PGD) [2, 3] to the frequency-domain heat equation. Combined with the reciprocity principle, this allows real-time evaluation of the temperature at a specific point of a thermal system in the online stage. More specifically, the PGD computes for all range of frequencies a *generalized transfer function* solution of the frequency-domain heat equation.

Thus a strategy based on an offline and online phase is designed. In the offline phase the previously cited generalized transfer function is computed at the desired monitoring point. Then, given the external heat source excitation, a convolution is used to determine online and in real-time the temperature at the desired monitoring point for any instant. As it will be shown, the online approximation is so fast that it can be used for control purposes in real-time and on deployed devices. This opens vast possibilities related to real-time simulation-based monitoring and control [4].

Representations in the frequency domain are appealing for analyzing responses of structures subjected to dynamic excitations. It is a powerful approach to study the response of structural systems when initial conditions can be neglected; that is, far enough from the initial transient response. This framework, which was integrated into the finite element framework from the very beginning, has been, and still is, extensively used. It is well described in most textbooks, some of them linked to many generations of scientists and engineers [5–8]. This approach is even now an active research area because several challenges are still open. For instance, separated representations in the frequency domain were considered in [9–17] for the so-called: *variational theory of complex rays*. Obviously, there have been many attempts considering such descriptions within the model reduction framework; the interested reader can refer to [18] and the references therein. This however is not the aim of the present paper, thus, no exhaustive state-of-the-art on this topic is presented.

Finally, it is important to note that in spite of the large amount of scientific contributions using a frequency domain description in solid dynamics, this approach is not standard, to the author's knowledge, for thermal models subjected to dynamical forced thermal loads. Certainly, time domain approximations of thermal models are both efficient and robust and, moreover, model order reduction is successfully applied in this setting [19–26]. Whereas frequency domain approaches for thermal studies are scarce [27–31].

## 2. MONITORING TEMPERATURE AT A SURFACE POINT

This section analyzes the representation of temperature at an arbitrary point of the boundary under an arbitrary transient external excitation, for instance, a traveling external heat source such as a moving laser. More specifically, the representation of the solution at the point of interest is first studied by means of a Green's function in the space-time domain. Then the applicability of the reciprocity principle for the transient heat equation with a forced excitation is discussed both in time and frequency domain. The use of reciprocity (only valid in the frequency domain) allows determining a representation of temperature at the desired point for any arbitrary external heat source.

### 2.1. Model problem in the space-time domain

Formally, the problem under consideration is described as follows. Given a time interval $I := ]0, T[$ ($T$ can be taken arbitrarily large) and a body $\Omega \subset \mathbb{R}^d, d \leq 3$, whose boundary $\partial \Omega$ is partitioned into Dirichlet, $\Gamma_D$, and Robin/Neumann, $\Gamma_N$, frontiers such that $\overline{\partial \Omega} = \overline{\Gamma}_D \cup \overline{\Gamma}_N$ and $\Gamma_D \cap \Gamma_N = \emptyset$; temperature evolution $u(\boldsymbol{x}, t)$, for $\boldsymbol{x} \in \Omega$ and $t \in I$, is described by the transient heat equation:

$$\begin{cases} \rho c_p \partial_t u - \nabla \cdot \mathbf{K} \nabla u = 0 & \text{in } \Omega \times I, \\ u = u_D & \text{on } \Gamma_D \times I, \\ \boldsymbol{n} \cdot \mathbf{K} \nabla u = -\ell(u - u_{\text{ext}}) + q & \text{on } \Gamma_N \times I, \\ u = u_0 & \text{on } \Omega \times \{0\}, \end{cases} \quad (1)$$

where $\rho$ is density (kg/m$^3$), $c_p$ is specific heat capacity (J/(kg K)), $\mathbf{K}$ is the thermal conductivity matrix (W/(m K)), $\ell$ is the heat transfer coefficient (W/(m$^2$ K)), $u_{\text{ext}}$ is the external temperature (K), $\boldsymbol{n}$ is the exterior unit normal to $\Gamma_N$ (dimensionless) and $q = q(\boldsymbol{x}, t)$, for $(\boldsymbol{x}, t) \in \Gamma_N \times I$, is the inflow forcing excitation (W/m$^2$). The international system of units of measurement is also employed for length (m) and time (s).

As noted in the introduction, $q$ is typically the heat flux imposed by a laser. The objective here is to determine a (fast) computable representation of the temperature at an arbitrary boundary point $\boldsymbol{x}_0 \in \Gamma_N$ and at any instant $t_0$, with $0 < t_0 < T$.

Since the problem is linear, (1) is further simplified. Thermal diffusivity (thermal conductivity divided by density and specific heat capacity) can be considered the only material constant in the partial differential equation. Moreover, the increment of temperature with respect to the external one, i.e. $(u - u_{\text{ext}})$, can be defined as the unknown of the problem (in practice, impose $u_{\text{ext}} = 0$).

Finally, for the clarity of the presentation, the model problem studied is further simplified. However, these simplifications (considering unitary values of the coefficients) do not compromise the validity of the following developments.

More precisely, the following assumptions are used to define the model problem: homogeneous Dirichlet boundary conditions, canonical dimensionless form with an isotropic homogeneous material, and no convective heat exchanges. Note however, that these simplifications, are only done to simplify the presentation and do not hinder the application of the proposed methodology to real problems described by (1) as it will be shown in Section 5. Under these assumptions, problem (1) becomes

$$\begin{cases} \partial_t u - \nabla^2 u = 0 & \text{in } \Omega \times I, \\ u = 0 & \text{on } \Gamma_D \times I, \\ \boldsymbol{n} \cdot \nabla u = q & \text{on } \Gamma_N \times I, \\ u = u_0 & \text{on } \Omega \times \{0\}. \end{cases} \quad (2)$$

### 2.2. Green's function and reciprocity in the space-time domain

The objective is to obtain the solution at an arbitrary point and time, $(\boldsymbol{x}_0, t_0)$. Ideally the desired value $u(\boldsymbol{x}_0, t_0)$ could be readily evaluated if the adjoint Green's function were known. The adjoint Green's function is the solution of

$$\begin{cases} \partial_t G + \nabla^2 G = 0 & \text{in } \Omega \times ]0, t_0[, \\ G = 0 & \text{on } \Gamma_D \times ]0, t_0[, \\ \boldsymbol{n} \cdot \nabla G = \delta(\boldsymbol{x} - \boldsymbol{x}_0)\delta(t - t_0) & \text{on } \Gamma_N \times ]0, t_0[, \\ G = 0 & \text{on } \Omega \times [t_0, T[, \end{cases} \quad (3)$$

where the notation of $G(\boldsymbol{x}, t; \boldsymbol{x}_0, t_0)$ clearly identifies the parametric dependence on $(\boldsymbol{x}_0, t_0)$. The representation of the desired temperature is then

$$u(\boldsymbol{x}_0, t_0) = \int_{\Gamma_N} \int_0^{t_0} G(\boldsymbol{x}, t; \boldsymbol{x}_0, t_0) \, q(\boldsymbol{x}, t) dt d\Gamma + \int_\Omega u_0(\boldsymbol{x}) \, G(\boldsymbol{x}, 0; \boldsymbol{x}_0, t_0) d\Omega.$$

See Appendix A for a detailed presentation. However, in general, the computation of the Green's function is by no means a trivial task, for instance when confronted to an arbitrary domain or inhomogeneous material properties. Consequently, this approach is not used in practice.

An alternative is to use the reciprocity property [1, 32, 33]. However, it is also well-known that it is not applicable to the heat equation because the operator is not self-adjoint. In order to recall this, the variational problem equivalent to (2) is presented: find $u \in \mathcal{S}$ such that

$$B(u, v) = L(q; v) \quad \forall v \in \mathcal{V}, \tag{4}$$

with the appropriate spaces introducing the required regularity in space and time [34, 35]

$$\mathcal{V} := \big\{ v : v(\cdot, t) \in \mathcal{H}^1(\Omega),\, v(\boldsymbol{x}, \cdot) \in \mathcal{L}^2(I),\, v = 0 \text{ on } \Gamma_D \times I \big\}$$
$$\cap \big\{ v : v(\cdot, t) \in \mathcal{H}^{-1}(\Omega),\, v(\boldsymbol{x}, \cdot) \in \mathcal{H}^1(I) \big\},$$
$$\mathcal{S} := \big\{ v : v \in \mathcal{V},\, v(\boldsymbol{x}, 0) = u_0 \big\},$$

and

$$B(u, v) = \int_\Omega \int_I v\, \partial_t u\, dt d\Omega + \int_\Omega \int_I \nabla u \cdot \nabla v\, dt d\Omega, \quad L(q; v) = \int_{\Gamma_N} \int_I qv\, dt d\Gamma.$$

Given two excitations $q_1$ and $q_2$, the corresponding solutions of Eq. (4) are denoted $u_1$ and $u_2$, respectively. Since both $u_1$ and $u_2$ belong to $\mathcal{S} \subset \mathcal{V}$ the following expressions are also verified:

$$B(u_1, u_2) = L(q_1; u_2) \text{ and } B(u_2, u_1) = L(q_2; u_1). \tag{5}$$

However, the bilinear form is non-symmetric because of the time derivative, i.e. $B(u, v) \neq B(v, u)$. Thus, subtracting both expressions in Eq. (5), standard reciprocity is not satisfied because the left hand side terms do not cancel out. In conclusion,

$$L(q_1; u_2) \neq L(q_2; u_1).$$

Therefore, in the space-time domain a Green's function approach or a reciprocity property cannot be used in practice to determine temperature at a surface point and instance, say $(\boldsymbol{x}_0, t_0) \in \Gamma_N \times I$.

### 2.3. Space-frequency problem for an arbitrary excitation

Another alternative for studying this forced excitation problem is to consider harmonic analysis. In order to work in the frequency domain the Fourier transform and its inverse are used, namely

$$\hat{v}(\boldsymbol{x}, \omega) = \mathcal{F}[v] = \int_{-\infty}^{+\infty} v(\boldsymbol{x}, t)\, e^{-i\omega t} dt \tag{6a}$$

and

$$v(\boldsymbol{x}, t) = \mathcal{F}^{-1}[\hat{v}] = \frac{1}{2\pi} \int_{-\infty}^{+\infty} \hat{v}(\boldsymbol{x}, \omega)\, e^{i\omega t} d\omega. \tag{6b}$$

*Remark 1* (Fourier transform properties)
Fourier transforms have been largely studied and they hold a large number of properties (viz. linearity, translation, etc). In what follows it is important to recall that, in general, $\hat{v} \in \mathbb{C}$; but, for an even function in time $v_e$, i.e. $v_e(\boldsymbol{x}, -t) = v_e(\boldsymbol{x}, t)$, $\mathcal{F}[v_e] = \hat{v}_e \in \mathbb{R}$; whereas, for an odd function in time $v_o$, i.e. $v_o(\boldsymbol{x}, -t) = -v_o(\boldsymbol{x}, t)$, $\mathcal{F}[v_o]$ is imaginary, i.e. $\mathcal{F}[v_o] \in i\mathbb{R}$. For an odd function in time $v_o$, $\hat{v}_o$ is redefined as the imaginary part of $\mathcal{F}[v_o]$. Thus, $\mathcal{F}[v_o] = i\hat{v}_o$ with $\hat{v}_o \in \mathbb{R}$.

Applying the Fourier transform to problem (2), it becomes

$$\begin{cases} i\omega\hat{u} - \nabla^2\hat{u} = 0 & \text{in } \Omega, \\ \hat{u} = 0 & \text{on } \Gamma_D, \\ \boldsymbol{n} \cdot \nabla\hat{u} = \hat{q} & \text{on } \Gamma_N. \end{cases} \tag{7}$$

*Remark 2* (Long-term forced solution)
Note that the harmonic solution is only concerned with the long-term forced solution and consequently it does not depend on the initial condition. Standard approaches should be used for evaluating the transient regime, which, in practice, decays rapidly to the obtained long-term solution.

The variational form associated to the strong form problem described in (7) reads: find $\hat{u} \in \mathcal{H}^1_{\Gamma_D} := \{ v \in \mathcal{H}^1(\Omega) : v = 0 \text{ on } \Gamma_D \}$ such that

$$\big(\nabla\hat{u}, \nabla\hat{v}\big) + i\omega\big(\hat{u}, \hat{v}\big) = \langle\hat{q}, \hat{v}\rangle \quad \forall\hat{v} \in \mathcal{H}^1_{\Gamma_D}, \tag{8}$$

where

$$\big(\hat{u}, \hat{v}\big) = \int_\Omega \hat{u}\,\hat{v}^*\,d\Omega \,, \; \big(\nabla\hat{u}, \nabla\hat{v}\big) = \int_\Omega \nabla\hat{u} \cdot \nabla\hat{v}^*\,d\Omega \text{ and } \langle\hat{u}, \hat{v}\rangle = \int_{\Gamma_N} \hat{u}\,\hat{v}^*\,d\Gamma \tag{9}$$

denote, respectively, the $\mathcal{L}^2$ scalar product of functions $\hat{u}$ and $\hat{v}$ and gradients in $\Omega$ and its traces over $\Gamma_N$. Note also, that $\hat{v}^*$ indicates the complex conjugate of $\hat{v}$, since both $\hat{u}$ and $\hat{v}$ are, in general, in $\mathbb{C}$.

It is important to observe that Eq. (8) is non-Hermitian but it is symmetric, the later property proves sufficient and also crucial for reciprocity.

### 2.4. Arbitrary excitation implies solving two problems with real excitation

Given any arbitrary excitation, $q(\boldsymbol{x}, t)$, it can always be decomposed in the sum of an even and odd function, namely

$$q(\boldsymbol{x}, t) = q_e(\boldsymbol{x}, t) + q_o(\boldsymbol{x}, t) = \frac{1}{2}\big(q(\boldsymbol{x}, t) + q(\boldsymbol{x}, -t)\big) + \frac{1}{2}\big(q(\boldsymbol{x}, t) - q(\boldsymbol{x}, -t)\big).$$

Recalling the Fourier transform properties: $\mathcal{F}[q] = \hat{q} = \mathcal{F}[q_e] + \mathcal{F}[q_o] = \hat{q}_e + i\hat{q}_o$ with $\hat{q}_e(\boldsymbol{x}, \omega) \in \mathbb{R}$ and $\hat{q}_o(\boldsymbol{x}, \omega) \in \mathbb{R}$. Moreover, it is important to notice that, the decomposition of $q(\boldsymbol{x}, t)$ in the sum of an even and odd excitation produces two identical problems with a real excitation whose solutions are the real and the imaginary part of the solution of (7). More precisely, because of the linearity of (7) and Remark 3, the solution $\hat{u}$ of (7) can be decomposed as $\hat{u} = \hat{u}_e + i\hat{u}_o$, with $\hat{u}_e$ and $\hat{u}_o$ solutions of

$$\begin{cases} i\omega\hat{u}_e - \nabla^2\hat{u}_e = 0 & \text{in } \Omega, \\ \hat{u}_e = 0 & \text{on } \Gamma_D, \text{ and} \\ \boldsymbol{n} \cdot \nabla\hat{u}_e = \hat{q}_e & \text{on } \Gamma_N, \end{cases} \begin{cases} i\omega\hat{u}_o - \nabla^2\hat{u}_o = 0 & \text{in } \Omega, \\ \hat{u}_o = 0 & \text{on } \Gamma_D, \\ \boldsymbol{n} \cdot \nabla\hat{u}_o = \hat{q}_o & \text{on } \Gamma_N. \end{cases} \tag{10}$$

Then, the original solution in the time domain can be recovered by means of the inverse Fourier transform, namely $u = \mathcal{F}^{-1}[\hat{u}] = \mathcal{F}^{-1}[\hat{u}_e] + \mathcal{F}^{-1}[i\hat{u}_o] = u_e + u_o$.

In summary, it is possible to find the solution of (7) —or (8)— for any arbitrary excitation $\hat{q}$ solving twice the same problem but with different *real* excitations, one corresponding to $\hat{q}_e(\boldsymbol{x}, \omega)$ and the other to $\hat{q}_o(\boldsymbol{x}, \omega)$.

*Remark 3* (Imaginary excitation)
Suppose $u$ is solution of the following problem

$$\begin{cases} i\omega u - \nabla^2 u = 0 & \text{in } \Omega, \\ u = 0 & \text{on } \Gamma_D, \\ \boldsymbol{n} \cdot \nabla u = q & \text{on } \Gamma_N. \end{cases}$$

Then, $v = iu$ is solution of

$$\begin{cases} i\omega v - \nabla^2 v = 0 & \text{in } \Omega, \\ v = 0 & \text{on } \Gamma_D, \\ \boldsymbol{n} \cdot \nabla v = iq & \text{on } \Gamma_N. \end{cases}$$

Hint: replace $u = -iv$ in the first problem and obtain the second one. Obviously, this follows directly from linearity but it is explicitly recalled for didactic purposes.

### 2.5. Reciprocity in space-frequency holds for a real excitation

Given two real harmonic excitations $\hat{q}_1$ and $\hat{q}_2$, the corresponding solutions of (8) are denoted by $\hat{u}_1$ and $\hat{u}_2$, respectively. Then, since both solutions belong to $\mathcal{H}^1_{\Gamma_D}$, the following expressions hold:

$$\big(\nabla\hat{u}_1, \nabla\hat{u}_2\big) + i\omega\big(\hat{u}_1, \hat{u}_2\big) = \big\langle\hat{q}_1, \hat{u}_2\big\rangle, \tag{11a}$$

$$\big(\nabla\hat{u}_2, \nabla\hat{u}_1\big) + i\omega\big(\hat{u}_2, \hat{u}_1\big) = \big\langle\hat{q}_2, \hat{u}_1\big\rangle. \tag{11b}$$

Substracting (11b) from (11a) gives

$$\big(\nabla\hat{u}_1, \nabla\hat{u}_2\big) - \big(\nabla\hat{u}_2, \nabla\hat{u}_1\big) + i\omega\big[\big(\hat{u}_1, \hat{u}_2\big) - \big(\hat{u}_2, \hat{u}_1\big)\big] = \big\langle\hat{q}_1, \hat{u}_2\big\rangle - \big\langle\hat{q}_2, \hat{u}_1\big\rangle, \tag{12}$$

which clearly shows that reciprocity is satisfied in the frequency domain, namely

$$\big\langle\hat{q}_1, \hat{u}_2\big\rangle = \big\langle\hat{q}_2, \hat{u}_1\big\rangle, \tag{13}$$

if the following conditions hold

$$\big(\nabla\hat{u}_1, \nabla\hat{u}_2\big) = \big(\nabla\hat{u}_2, \nabla\hat{u}_1\big) \text{ and } \big(\hat{u}_1, \hat{u}_2\big) = \big(\hat{u}_2, \hat{u}_1\big). \tag{14}$$

This is precisely the case when $\hat{q}_1$ and $\hat{q}_2$ are real. See Appendix B for a detailed proof of Eqs. (13).

*Remark 4* (Reciprocity with convective heat flux)
In the general case when convective heat fluxes are considered, see (1), reciprocity also holds. Linearity is exploited solving for $(u - u_{\text{ext}})$ instead of the original temperature $u$. Accordingly, equations (11) are modified as follows:

$$\big(\nabla\hat{u}_1, \nabla\hat{u}_2\big) + i\omega\big(\hat{u}_1, \hat{u}_2\big) + \big\langle\ell\hat{u}_1, \hat{u}_2\big\rangle = \big\langle\hat{q}_1, \hat{u}_2\big\rangle,$$

$$\big(\nabla\hat{u}_2, \nabla\hat{u}_1\big) + i\omega\big(\hat{u}_2, \hat{u}_1\big) + \big\langle\ell\hat{u}_2, \hat{u}_1\big\rangle = \big\langle\hat{q}_2, \hat{u}_1\big\rangle.$$

Subtracting both equations shows that reciprocity also holds for convective heat because the same conditions described by (14) are obtained. Note that if (14) are verified then symmetry also hold for the traces, i.e. $\big\langle\hat{u}_1, \hat{u}_2\big\rangle = \big\langle\hat{u}_2, \hat{u}_1\big\rangle$.

### 2.6. Using reciprocity to monitor temperature

Recall that the final objective is to monitor temperature at a given point for an arbitrary external excitation, i.e. evaluate $u(\boldsymbol{x}_0, t_0)$ for $(\boldsymbol{x}_0, t_0) \in \Gamma_N \times I$. For this purpose, it is necessary to determine $\hat{u}(\boldsymbol{x}_0, \omega)$ for an arbitrary external excitation, $\hat{q}$, in the space-frequency domain. The conclusion of Section 2.4 is that two problems, which are shown in strong form by (10), with real excitations $\hat{q}_e$ and $\hat{q}_o$, such that $\hat{q} = \hat{q}_e + i\hat{q}_o$, must be solved to find $\hat{u}(\boldsymbol{x}_0, \omega) = \hat{u}_e(\boldsymbol{x}_0, \omega) + i\hat{u}_o(\boldsymbol{x}_0, \omega)$.

Suppose, that for each frequency, $\omega \in \mathbb{R}$, one could also determine the corresponding solution $\hat{h}(\boldsymbol{x}, \omega; \boldsymbol{x}_0)$ under a Dirac flux imposed at the monitoring point $\boldsymbol{x}_0$, $\delta(\boldsymbol{x} - \boldsymbol{x}_0)$, namely

$$\begin{cases} i\omega\hat{h} - \nabla^2\hat{h} = 0 & \text{in } \Omega, \\ \hat{h} = 0 & \text{on } \Gamma_D, \\ \boldsymbol{n} \cdot \nabla\hat{h} = \delta(\boldsymbol{x} - \boldsymbol{x}_0) & \text{on } \Gamma_N. \end{cases} \tag{15}$$

Since all excitations are real, reciprocity, see (13), holds and consequently

$$\big\langle\delta(\boldsymbol{x} - \boldsymbol{x}_0), \hat{u}_e\big\rangle = \big\langle\hat{q}_e, \hat{h}\big\rangle \text{ and } \big\langle\delta(\boldsymbol{x} - \boldsymbol{x}_0), \hat{u}_o\big\rangle = \big\langle\hat{q}_o, \hat{h}\big\rangle,$$

that is,

$$\hat{u}_e(\boldsymbol{x}_0, \omega) = \big\langle\hat{h}(\cdot, \omega; \boldsymbol{x}_0), \hat{q}_e(\cdot, \omega)\big\rangle \text{ and } \hat{u}_o(\boldsymbol{x}_0, \omega) = \big\langle\hat{h}(\cdot, \omega; \boldsymbol{x}_0), \hat{q}_o(\cdot, \omega)\big\rangle.$$

This implies, see Remark 5, that

$$\hat{u}(\boldsymbol{x}_0, \omega) = \int_{\Gamma_N} \hat{h}(\boldsymbol{x}, \omega; \boldsymbol{x}_0)\, \hat{q}(\boldsymbol{x}, \omega)\, d\Gamma. \tag{16}$$

Once temperature is monitored at the desired point in the space-frequency domain, the inverse Fourier transform is employed to obtain the desired final representation of temperature in the space-time domain:

$$u(\boldsymbol{x}_0, t) = \mathcal{F}^{-1}\big[\hat{u}(\boldsymbol{x}_0, \omega)\big] = \int_{\Gamma_N} \mathcal{F}^{-1}\big[\hat{h}(\boldsymbol{x}, \omega; \boldsymbol{x}_0)\, \hat{q}(\boldsymbol{x}, \omega)\big]\, d\Gamma.$$

This expression can be further simplified using the *convolution theorem* [36, 37], recall

$$\mathcal{F}^{-1}\big[\hat{h}(\boldsymbol{x}, \omega; \boldsymbol{x}_0)\, \hat{q}(\boldsymbol{x}, \omega)\big] = \int_0^t h(\boldsymbol{x}, \tau; \boldsymbol{x}_0)\, q(\boldsymbol{x}, t - \tau) d\tau,$$

where

$$h(\boldsymbol{x}, \tau; \boldsymbol{x}_0) = \mathcal{F}^{-1}[\hat{h}](\boldsymbol{x}, \tau; \boldsymbol{x}_0) = \frac{1}{2\pi} \int_{-\infty}^{+\infty} \hat{h}(\boldsymbol{x}, \omega; \boldsymbol{x}_0)\, e^{i\omega t} d\omega. \tag{17}$$

Thus, the representation of the temperature at the desired point $\boldsymbol{x}_0 \in \Gamma_N$ is

$$u(\boldsymbol{x}_0, t) = \int_{\Gamma_N} \int_0^t \left( \frac{1}{2\pi} \int_{-\infty}^{+\infty} \hat{h}(\boldsymbol{x}, \omega; \boldsymbol{x}_0)\, e^{i\omega t} d\omega \right) q(\boldsymbol{x}, t - \tau)\, d\tau d\Gamma,$$

which can be written in a more compact form and for any instance $t_0 \in I = ]0, T[$ as

$$u(\boldsymbol{x}_0, t_0) = \int_0^{t_0} \big\langle h(\cdot, \tau; \boldsymbol{x}_0), q(\cdot, t_0 - \tau) \big\rangle\, d\tau. \tag{18}$$

Recall that $q \in \mathbb{R}$.

This is a compact and useful expression, it only requires knowledge of the external imposed excitation $q$ up to the desired monitored instant $t_0$ (causality). Moreover, and this is a major point and advantage, (18) does not reflect the decomposition of the excitation in even and odd contributions. Thus, if the transfer function, $h(\boldsymbol{x}, \tau; \boldsymbol{x}_0)$, is known, (18) can be applied directly for any arbitrary excitation $q(\boldsymbol{x}, t)$.

However this expression also presents a major drawback: the inverse Fourier transform of $\hat{h}$, solution of (15), must be known. This implies solving (15) for every frequency $\omega$ in the range needed by the arbitrary excitation. Thus, in general, the representation (18) cannot be used in practice.

The next section circumvents this drawback and proposes a methodology to obtain an expression for the generalized transfer function $\hat{h}$, solution of (15), for the all range of realistic frequencies. This expression can then be substituted in (18) to determine the desired temperature. Moreover, (18) can be evaluated in real-time.

*Remark 5* (Reconstruction of solution)
To determine (16) it is important to recall that $\hat{q}_e$ and $\hat{q}_o$ are real. Thus, the scalar products on $\Gamma_N$,

$$\hat{u}(\boldsymbol{x}_0, \omega) = \hat{u}_e(\boldsymbol{x}_0, \omega) + i\hat{u}_o(\boldsymbol{x}_0, \omega) = \big\langle \hat{h}(\cdot, \omega; \boldsymbol{x}_0), \hat{q}_e(\cdot, \omega) \big\rangle + i\big\langle \hat{h}(\cdot, \omega; \boldsymbol{x}_0), \hat{q}_o(\cdot, \omega) \big\rangle,$$

can be rewritten as

$$\hat{u}(\boldsymbol{x}_0, \omega) = \int_{\Gamma_N} \hat{h}(\boldsymbol{x}, \omega; \boldsymbol{x}_0)\, \hat{q}_e(\boldsymbol{x}, \omega)\, d\Gamma + i \int_{\Gamma_N} \hat{h}(\boldsymbol{x}, \omega; \boldsymbol{x}_0)\, \hat{q}_o(\boldsymbol{x}, \omega)\, d\Gamma$$

$$= \int_{\Gamma_N} \hat{h}(\boldsymbol{x}, \omega; \boldsymbol{x}_0)\big(\hat{q}_e(\boldsymbol{x}, \omega) + i\hat{q}_o(\boldsymbol{x}, \omega)\big) d\Gamma = \int_{\Gamma_N} \hat{h}(\boldsymbol{x}, \omega; \boldsymbol{x}_0)\, \hat{q}(\boldsymbol{x}, \omega)\, d\Gamma,$$

and do not present any complex conjugate. In fact, it is important to note that

$$\hat{u}(\boldsymbol{x}_0, \omega) = \int_{\Gamma_N} \hat{h}(\boldsymbol{x}, \omega; \boldsymbol{x}_0)\, \hat{q}(\boldsymbol{x}, \omega)\, d\Gamma = \big\langle \hat{h}(\cdot, \omega; \boldsymbol{x}_0), \hat{q}^*(\cdot, \omega) \big\rangle \neq \big\langle \hat{h}(\cdot, \omega; \boldsymbol{x}_0), \hat{q}(\cdot, \omega) \big\rangle.$$

*Remark 6* (Inverse Fourier Transform of the generalized transfer function)
The inverse fourier transform of the *generalized transfer function*, $\hat{h}(\boldsymbol{x}, \omega; \boldsymbol{x}_0)$, see (17) is computed using the FFT algorithm. Only periodic signals with a finite number of harmonics can be exactly represented with the discrete Fourier transform, and thus non-periodic signals involving a continuous spectrum of frequencies can only be approximated. The range of frequencies included in the generalized transfer function must be chosen accordingly.

*Remark 7* (Convective heat flux)
In the general case described in (1), when convective fluxes are present, the generalized transfer function problem originally described by (15) is modified. As noted in Remark 4, reciprocity also holds when convective fluxes are considered. Thus, the generalized transfer function must have on the Neumann boundary the convective heat flux, namely

$$\begin{cases} i\omega\hat{h} - \nabla^2\hat{h} = 0 & \text{in } \Omega, \\ \hat{h} = 0 & \text{on } \Gamma_D, \\ \boldsymbol{n} \cdot \nabla\hat{h} = -\ell\hat{h} + \delta(\boldsymbol{x} - \boldsymbol{x}_0) & \text{on } \Gamma_N. \end{cases}$$

Following the procedure described previously, equations (16) and (18) also hold.

## 3. COMPUTING THE GENERALIZED TRANSFER FUNCTION

This section is aimed at computing a generalized transfer function, $\hat{h}(\boldsymbol{x}, \omega; \boldsymbol{x}_0)$, for a desired and predefined range of frequencies, $I_\omega$. This transfer function needs to be computed only once, and preferably offline. Since it is determined in the frequency domain, its inverse Fourier transform is later evaluated in order to use equation (18) as a simple and inexpensive post-process of any given excitation $q(\boldsymbol{x}, t)$.

A major contribution of the PGD approach is to view frequency, $\omega$, as a new coordinate [4]. Thus, instead of solving problem (15) for each frequency, the objective is to solve, only once, a more general problem with $\omega$ as an extra coordinate, namely find $\hat{h}(\boldsymbol{x}, \omega; \boldsymbol{x}_0)$ satisfying

$$\begin{cases} i\omega\hat{h} - \nabla^2\hat{h} = 0 & \text{in } \Omega \times I_\omega, \\ \hat{h} = 0 & \text{on } \Gamma_D \times I_\omega, \\ \boldsymbol{n} \cdot \nabla\hat{h} = \delta(\boldsymbol{x} - \boldsymbol{x}_0) & \text{on } \Gamma_N \times I_\omega, \end{cases} \tag{19}$$

where $I_\omega$ is the predefined range of variation of $\omega$. The increased dimensionality is the price to pay. However, as shown numerically in [4] and references therein, the complexity of the PGD does not grow exponentially with the space dimension. On the contrary, numerical evidence shows that it scales linearly for a moderate number of dimensions. This is precisely what happens in this problem when $\omega$ is introduced as an extra coordinate. This is obvious for each resolution of the greedy algorithm. However, for large number of dimensions ($> 100$) or in non-symmetric problems the number of terms required for a given precision is sensible to the number of dimensions.

The weak problem equivalent to (19) is obtained using a weighted residual argument, namely, find $\hat{h}$ for all $\hat{v}$ in the selected appropriate functional space such that

$$A(\hat{h}, \hat{v}) = L(\hat{v}) \tag{20a}$$

with

$$A(\hat{h}, \hat{v}) := \int_{I_\omega} \big(\nabla\hat{h}, \nabla\hat{v}\big)d\omega + \int_{I_\omega} i\omega\big(\hat{h}, \hat{v}\big)d\omega \tag{20b}$$

$$L(\hat{v}) := \int_{I_\omega} \hat{v}^*(\boldsymbol{x}_0, \omega)d\omega. \tag{20c}$$

Note that formally, the required functional spaces must account for the singularity of the Dirac flux. Nevertheless, in practice, the Dirac delta is mollified and this allows to use the standard finite element functional setup.

The PGD approach assumes that the solution of (20), $\hat{h}(\boldsymbol{x}, \omega; \boldsymbol{x}_0)$, can be approximated by a rank-n separable function, $\hat{h}^n(\boldsymbol{x}, \omega; \boldsymbol{x}_0)$, namely,

$$\hat{h}(\boldsymbol{x}, \omega; \boldsymbol{x}_0) \approx \hat{h}^n(\boldsymbol{x}, \omega; \boldsymbol{x}_0) = \sum_{s=1}^{n} X^s(\boldsymbol{x}) W^s(\omega) = \hat{h}^{n-1}(\boldsymbol{x}, \omega; \boldsymbol{x}_0) + X^n(\boldsymbol{x}) W^n(\omega), \qquad (21)$$

where $X^s \in \mathcal{H}^1_{\Gamma_D}$ and $W^s \in \mathcal{L}^2(I_\omega)$ for $s = 1, \ldots, n$. Recall that these functions give values in $\mathbb{C}$.

A greedy algorithm [38] is used to construct this approximation, that is, to determine the unknown functions $X^s$ and $W^s$ in Eq. (21). In other words, a progressive scheme is designed to compute each new term with all the information at hand. The sequence is stopped with an appropriate error estimator [39–41]. Note that each new term implies the computation of a product of unknown functions, $X^n$ and $W^n$. Thus a nonlinear scheme must be designed. It is standard to use a fixed point alternating direction algorithm because it has proven robust in former works [3, 4, 42]. To simplify notation each iterate approximating $X^n$ and $W^n$ is denoted by $R$ and $S$. Hence, the nonlinear problem to solve for each new term of $\hat{h}^n(\boldsymbol{x}, \omega; \boldsymbol{x}_0)$ is obtained substituting (21) in (20a), in order to compute $R$ and $S$ (iterates of $X^n$ and $W^n$) such that

$$A(R\,S, \hat{v}) = L(\hat{v}) - A(\hat{h}^{n-1}, \hat{v}) \qquad (22)$$

with trial functions on the tangent manifold

$$\hat{v} = \hat{v}_R(\boldsymbol{x})\,S(\omega) + R(\boldsymbol{x})\,\hat{v}_S(\omega) \quad \forall \hat{v}_R \in \mathcal{H}^1_{\Gamma_D} \text{ and } \forall \hat{v}_S \in \mathcal{L}^2(I_\omega).$$

The alternating direction scheme, detailed below, consists in, for instance, updating the space function $R$ from a given $S$ assumed known, and then compute $S$ from the just updated function $R$. This iteration continues until reaching convergence of both $R$ and $S$. That is, the two stages for each iteration are:

1. Find $R \in \mathcal{H}^1_{\Gamma_D}$ ($S$ assumed known) such that

$$A(R\,S, \hat{v}_R\,S) = L(\hat{v}_R\,S) - A(\hat{h}^{n-1}, \hat{v}_R\,S) \quad \forall \hat{v}_R \in \mathcal{H}^1_{\Gamma_D}. \qquad (23a)$$

2. Find $S \in \mathcal{L}^2(I_\omega)$ ($R$ assumed known) such that

$$A(R\,S, R\,\hat{v}_S) = L(R\,\hat{v}_S) - A(\hat{h}^{n-1}, R\,\hat{v}_S) \quad \forall \hat{v}_S \in \mathcal{L}^2(I_\omega). \qquad (23b)$$

Then at convergence, $X^n$ and $W^n$ are updated by $R$ and $S$.

### 3.1. Updating the space function

For each new term in the series defined by (21) and each iteration described by (23), equation (23a) must be solved. Taking advantage of the separated structure of the solution and also of $A(\cdot, \cdot)$, see (20b), equation (23a) can be rewritten as, find $R \in \mathcal{H}^1_{\Gamma_D}$ for all $\hat{v}_R \in \mathcal{H}^1_{\Gamma_D}$ ($S$ assumed known) such that

$$\alpha^S(\nabla R, \nabla \hat{v}_R) + i\beta^S(R, \hat{v}_R) = \gamma^S \hat{v}_R^*(\boldsymbol{x}_0) - \sum_{s=1}^{n-1} \alpha_s^S(\nabla X^s, \nabla \hat{v}_R) + i\beta_s^S(X^s, \hat{v}_R), \qquad (24)$$

where the coefficients, which must be computed for each instance of $S$, are defined as

$$\alpha^S = (S, S)_{I_\omega}, \beta^S = (\omega\,S, S)_{I_\omega}, \gamma^S = (1, S)_{I_\omega},$$
$$\alpha_s^S = (W^s, S)_{I_\omega}, \text{ and } \beta_s^S = (\omega\,W^s, S)_{I_\omega}.$$

Recall that $\left(\cdot,\cdot\right)_{I_\omega}$ denotes the $\mathcal{L}^2$ scalar product of complex functions in $I_\omega$.

After the corresponding discretization of the spatial domain with a standard combination of piecewise linear shape functions, the system of linear equations induced by (24) presents a conductivity and a mass matrix. These matrices are computed only once because they are constant for each iteration and for each term. Moreover, it is important to note that they are symmetric but non-Hermitian, which will preclude, for instance, Cholesky or conjugate gradient schemes.

### 3.2. Updating the frequency function

Similarly, the second stage, described by equation (23b), can also be rewritten using the separated structure of the solution and also of $A(\cdot,\cdot)$ as, find $S \in \mathcal{L}^2(I_\omega)$ for all $\hat{v}_S \in \mathcal{L}^2(I_\omega)$ ($R$ assumed known from the previous stage) such that

$$\alpha^R\left(S,\hat{v}_S\right)_{I_\omega} + i\beta^R\left(\omega\,S,\hat{v}_S\right)_{I_\omega} = \gamma^R\left(1,\hat{v}_S\right)_{I_\omega} - \sum_{s=1}^{n-1}\alpha_s^R\left(W^s,\hat{v}_S\right)_{I_\omega} + i\beta_s^R\left(\omega\,W^s,\hat{v}_S\right)_{I_\omega}, \quad (25)$$

where the coefficients, which must be computed for each instance of $R$, are defined as $\mathcal{L}^2$ products over the spatial domain,

$$\alpha^R = \left(\nabla R, \nabla R\right), \beta^R = \left(R, R\right), \gamma^R = R^*(\boldsymbol{x}_0),$$
$$\alpha_s^R = \left(\nabla X^s, \nabla R\right), \text{ and } \beta_s^R = \left(X^s, R\right).$$

The lack of derivatives with respect to $\omega$ in the problem (19) induces an point-wise algebraic equation for $S$. Piecewise discontinuous approximations of $S$ will induce uncoupled scalar equations. Whereas continuous approximations over the one-dimensional range of frequencies lead to a symmetric but non-Hermitian matrix on the left-hand-side of (25), as in the previous case.

## 4. EXTENSION TO MULTI-PARAMETRIC AND INVERSE PROBLEMS

The approach presented here has a potentiality that exceeds real-time monitoring of temperature at a given location and can also be used for other thermal studies such as optimization, inverse analysis, nondestructive testing, etc. Here, two simple extensions are presented.

### 4.1. Multi-parametric models

As a simple demonstrator, thermal conductivity is chosen as an extra parameter. The underlying idea, already exploited in [4, 43], is to solve multi-parametric models capitalizing the advantages of the PGD framework. A multi-parametric model is an extension of the procedure detailed in the previous section. Besides frequency as an extra-coordinate the generalized transfer function can encompass other parameters as extra coordinates. For instance, parameters characterizing the geometry, the constitutive behavior or the boundary conditions could be incorporated. The PGD methodology allows to compute efficiently a multi-parametric solution defined in a high-dimensional space (spatial coordinates, frequency and other parameters). Multi-parametric models are of great interest in science and engineering because they make possible real-time simulation, optimization and inverse analysis, as illustrated in [4, 44].

For instance, the thermal example that motivates this work can also be posed as an inverse analysis to find the actual conductivity of a certain material from the temperature provided by a thermocouple placed at location $\boldsymbol{x}_0$. Then, independently of the inverse identification method used, it is obvious that fast identification procedures can be envisaged if an approximation of temperature at the monitoring point $\boldsymbol{x}_0$ for any instance $t$ can be computed in real-time for any conductivity $k$, i.e. $u(\boldsymbol{x}_0, t, k)$.

This approach can also be used for nondestructive testing. The monitored temperature being different from the computed one (obtained with the undamaged material parameters) triggers the

inverse analysis to determine the "damaged" material parameter, which can be solved readily because a generalized solution for any material parameter is available.

The inverse problem is not solved in detail at this point because it is outside the scope of this work. Nevertheless, here, the generalized solution for any conductivity is provided. Once this solution is known, any standard inverse algorithm could be implemented. The key point is to determine the generalized transfer function, $\hat{h}$, for any value of the conductivity $k \in I_k$, where $I_k$ is the desired range of conductivities. Problem (19) is now rewritten with the new parameter, conductivity, considered as an extra-coordinate. Thus the new problem consist in finding $\hat{h}(\boldsymbol{x}, \omega, k; \boldsymbol{x}_0)$ that satisfies

$$\begin{cases} i\omega\hat{h} - \nabla \cdot (k\nabla\hat{h}) = 0 & \text{in } \Omega \times I_\omega \times I_k, \\ \hat{h} = 0 & \text{on } \Gamma_D \times I_\omega \times I_k, \\ \boldsymbol{n} \cdot k\nabla\hat{h} = \delta(\boldsymbol{x} - \boldsymbol{x}_0) & \text{on } \Gamma_N \times I_\omega \times I_k. \end{cases}$$

The PGD approach must now determine an approximation $\hat{h}^n(\boldsymbol{x}, \omega, k; \boldsymbol{x}_0)$ to the solution of the previous problem, namely

$$\hat{h}(\boldsymbol{x}, \omega, k; \boldsymbol{x}_0) \approx \hat{h}^n(\boldsymbol{x}, \omega, k; \boldsymbol{x}_0) = \sum_{s=1}^{n} X^s(\boldsymbol{x}) \, W^s(\omega) \, K^s(k),$$

where extra separated functions must be determined; more precisely, those directly linked to conductivity, namely $K^s(k)$ for $s = 1, \ldots, n$. The same greedy approach described earlier can be applied with now an extra stage in the nonlinear solve to determine each $K^s(k)$. Once the multi-parametric solution has been computed, it can be postprocessed in the same way explained in Section 2.6 in order to recover the solution at $\boldsymbol{x}_0$ and any time $t$. The objective is that temperature at the monitoring point $\boldsymbol{x}_0$ for any instance $t$ can be computed in real-time for any conductivity $k$; that is, equation (18) is extended to approximate $u(\boldsymbol{x}_0, t, k)$, namely

$$u(\boldsymbol{x}_0, t, k) = \mathcal{F}^{-1}[\hat{u}](\boldsymbol{x}_0, t, k) = \int_0^t \big\langle h(\cdot, \tau, k; \boldsymbol{x}_0), q(\cdot, t_0 - \tau) \big\rangle \, d\tau, \tag{26}$$

where $h = \mathcal{F}^{-1}[\hat{h}]$.

As noted earlier, the crucial point is to determine a reasonable approximation of the generalized transfer function $\hat{h}(\boldsymbol{x}, \omega, k; \boldsymbol{x}_0)$. The example presented in Section 5 is proposed to demonstrate that such an approximation can be evaluated.

### 4.2. Inverse problem: an amplitude time-modulated calibration of excitation

This inverse problem considers that the amplitude of the power given by a laser varies with time because of uncontrolled power supply and has to be calibrated. Suppose an excitation defined by $\alpha(t)q(\boldsymbol{x}, t)$ where, as assumed in previous sections, $q(\boldsymbol{x}, t)$ is given (and, thus, known) while its amplitude, which varies with time $\alpha(t)$ is not know. Temperature at the monitoring point $\boldsymbol{x}_0$ for any instance $t$ is obtained following the procedure described in Section 2.4 for this new excitation, equation (18) becomes

$$u(\boldsymbol{x}_0, t) = \int_0^t \alpha(t_0 - \tau) \int_{\Gamma_N} h(\boldsymbol{x}, \tau; \boldsymbol{x}_0) \, q(\boldsymbol{x}, t - \tau) \, d\Gamma d\tau.$$

Then, given a discretization of the unknown function $\alpha(t)$, for instance

$$\alpha(t) = \sum_{j=1}^{n_{\text{fit}}} \alpha_j N_j(t), \tag{27}$$

where $N_j(t)$ are known interpolation functions, the coefficients $\boldsymbol{\alpha} \in \mathbb{R}^{n_{\text{fit}}}$ can be determined by a least-squares technique. This implies solving the normal equations $\mathbf{A}\boldsymbol{\alpha} = \mathbf{b}$.
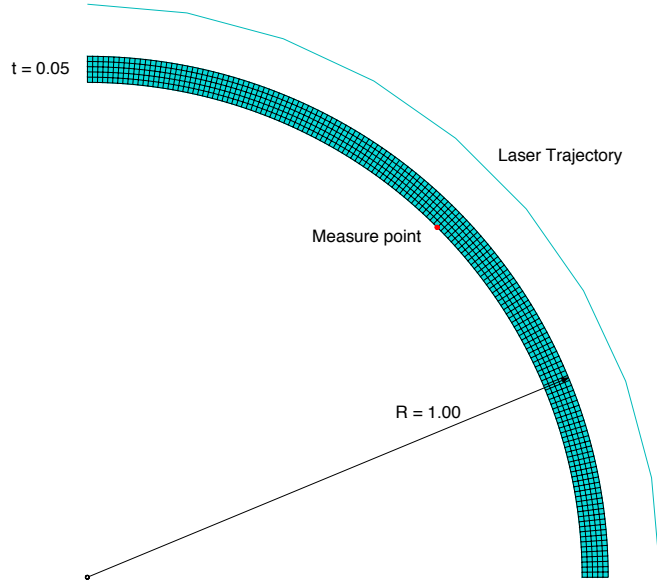
Figure 1. Single-ply composite cylinder: problem statement.

Given the series of instants $\{t_1, t_2, \ldots, t_m\}$ (with $m \geq n_{\text{fit}}$) at which temperature is going to be measured, the matrix of the normal equations is determined once and for all, during the *offline* phase, as

$$\mathbf{A} = [a_{ij}] = \left[ \sum_{r=1}^{m} \psi_i(t_r)\psi_j(t_r) \right]$$

with

$$\psi_i(t_r) = \int_0^{t_r} N_i(t_r - \tau) \int_{\Gamma_N} h(\boldsymbol{x}, \tau; \boldsymbol{x}_0)\, q(\boldsymbol{x}, t_r - \tau)\, d\Gamma d\tau.$$

Then, the measured values of temperature, $u^{\text{meas}}(\boldsymbol{x}_0, t_r)$, at $\boldsymbol{x}_0$ and for the series of instants $\{t_1, t_2, \ldots, t_m\}$ allow to compute, in the *online* phase, the independent term

$$\mathbf{b} = [b_i] = \left[ \sum_{r=1}^{m} \psi_i(t_r)u^{\text{meas}}(\boldsymbol{x}_0, t_r) \right].$$

Finally the normal equations $\mathbf{A}\boldsymbol{\alpha} = \mathbf{b}$ are solved.

## 5. NUMERICAL EXAMPLES

### 5.1. *Single-ply composite cylinder: verification of the proposed methodology*

Aiming to demonstrate the ability of the proposed method to monitor transient models, a 2D problem, which involves a heat flux moving over the outer boundary of a cylinder, is proposed. The outer boundary is also subjected to heat convection while the other boundaries are adiabatic. Figure 1 depicts the problem statement. The initial boundary value problem is described as

$$\begin{cases} \rho c_p \partial_t u - \nabla \cdot k\nabla u = 0 & \text{in } \Omega \times I, \\ \boldsymbol{n} \cdot k\nabla u = -\ell(u - u_{\text{ext}}) + q & \text{on } \Gamma_{\text{Out}} \times I, \\ \boldsymbol{n} \cdot k\nabla u = 0 & \text{on } \partial\Omega/\Gamma_{\text{Out}} \times I, \\ u = u_0 & \text{on } \Omega \times \{0\}, \end{cases} \tag{28}$$
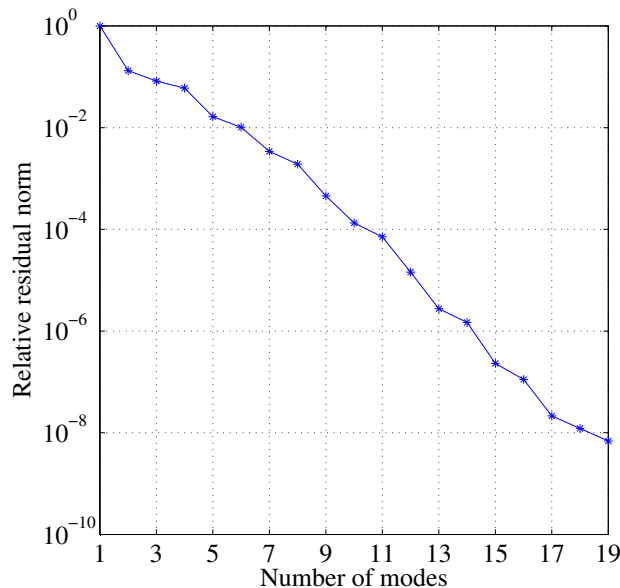
Figure 2. Single-ply composite cylinder: convergence of the generalized frequency transfer function.

where $\rho = 1\text{kg/m}^3$ is density, $c_p = 1\text{J/(kg K)}$ is specific heat capacity, $k = 1$ W/(m K) is isotropic thermal conductivity and $\ell = 1\text{W/(m}^2$ K) is the heat transfer coefficient, $u_{\text{ext}} = 298$K is the external temperature, $\Gamma_{\text{Out}}$ is the outer boundary where the laser impacts and with a radius of $1.0$m,

$$q(\xi, t) = 500 \exp\big(-50(2\xi - \pi t)^2\big)\text{W/m}^2 \tag{29}$$

is the inflow forcing excitation, and $\xi$ is the local tangent coordinate along $\Gamma_{\text{Out}}$. The temperature is measured (i.e. the point where temperature is monitored) at the middle point of the inner boundary. Finally, the thickness of the single-ply is $0.05$m.

The range of frequencies considered is $f \in [-250, 250]$ Hz or, in terms of the angular frequency used in all previous sections, $\omega \in I_\omega := [-500\pi, 500\pi]$. Such a large interval of frequencies has been chosen in order to be able to make a fair comparison with a reference solution. The time-step of a signal and the maximum frequency that can be computed from it are related by the Nyquist-Shannon theorem [45] as follows:

$$f_{\text{max}} = 1/2\Delta t. \tag{30}$$

The finite element (FE) reference solution is obtained with a standard time-marching Crank-Nicolson scheme whose time-step is chosen for accuracy considerations. In practice, a time-step of 2ms is accurate enough, and thus the maximum frequency to be considered is 250 Hz. With that frequency, the time signal recovered after performing the inverse Fourier transform has the same time-step as the FE reference solution.

The range $[-250, 250]$ Hz is clearly an overkill because the frequency range of the imposed heat flux $q$ is in $[-20, 20]$ Hz. This later range is determined because a Fourier transform of the heat flux seen by a point on $\Gamma_{\text{Out}}$ reveals that harmonics of frequency greater than 20 Hz transfer a negligible amount of energy to the system.

Moreover, note that for a particular negative frequency, the transfer function must be the complex conjugate of its symmetric (positive) counterpart. This is also a consequence of the Nyquist-Shannon theorem. Here negative frequencies are also computed to verify numerically that the PGD method reproduces a symmetric real part and an anti-symmetric imaginary part.

As discussed in Section 3 and depicted in (21), PGD is used to determine an approximation, say $\hat{h}^n$, of the transfer function, $\hat{h}$, solution of problem (19). In fact, Figure 2 shows the relative residue of (20) as the number of modes $n$ increases. The normalized residue is computed using the $\mathcal{L}^2$ norm of the discrete residue normalized by the norm of the rigth-hand-side of (20a).
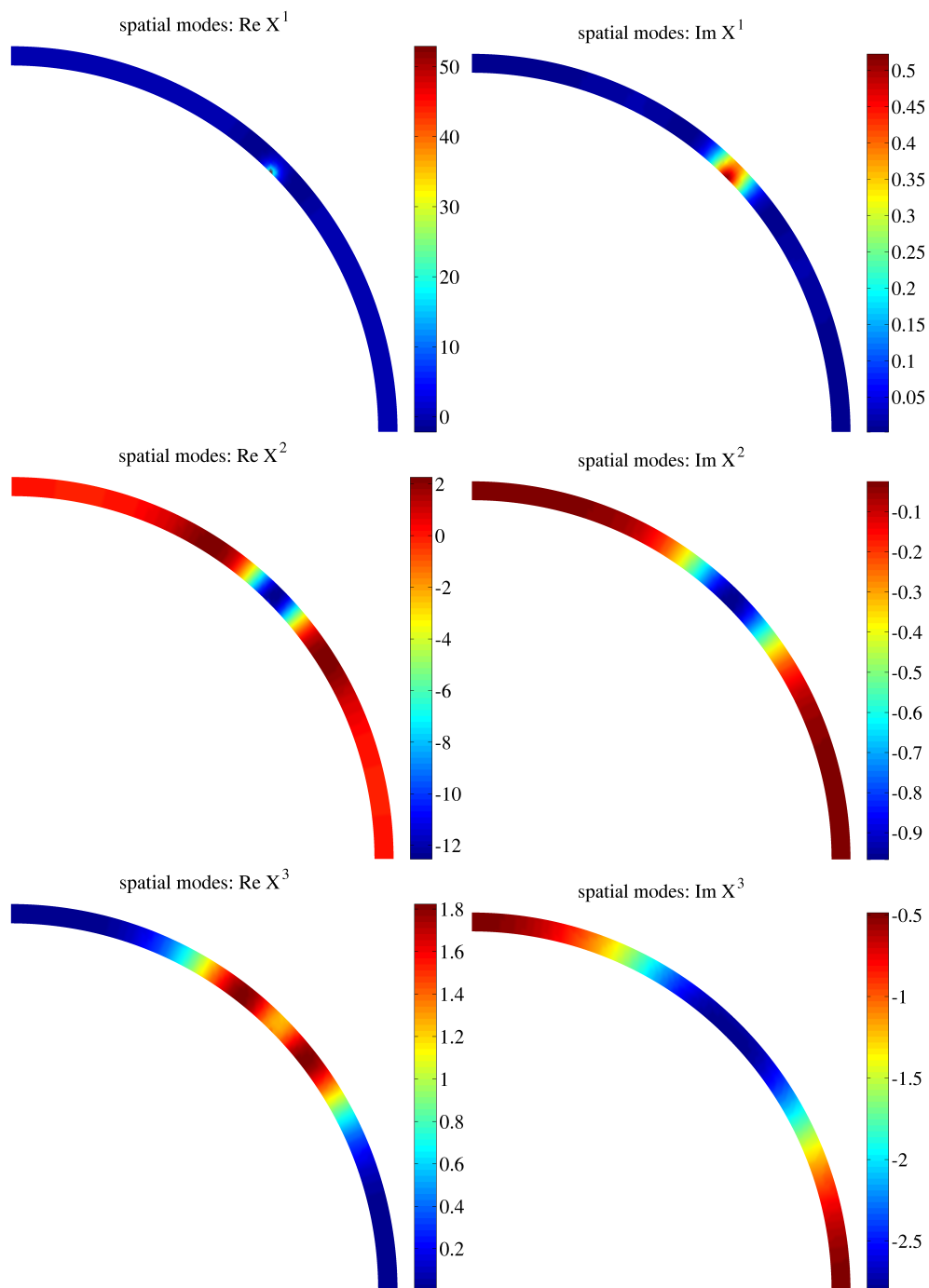
Figure 3. Single-ply composite cylinder: first 3 PGD spatial modes real (left) and imaginary (right).

For demonstration purposes tolerances are taken small, beyond engineering accuracy. However, 19 terms induce negligible (below $10^{-8}$!) normalized relative residues. The average number of fixed-point iterations is 25 (same tolerance of $10^{-8}$). Since 19 terms are necessary to reduce the residual norm below $10^{-8}$, the total amount of FE solves in the offline stage is around 475.

Note that spatial modes and frequency modes are localized. Figures 3 and 4 show respectively the first three spatial and frequency modes. These modes are $X^1$, $W^1$, $X^2$, $W^2$, $X^3$ and $W^3$. Since all
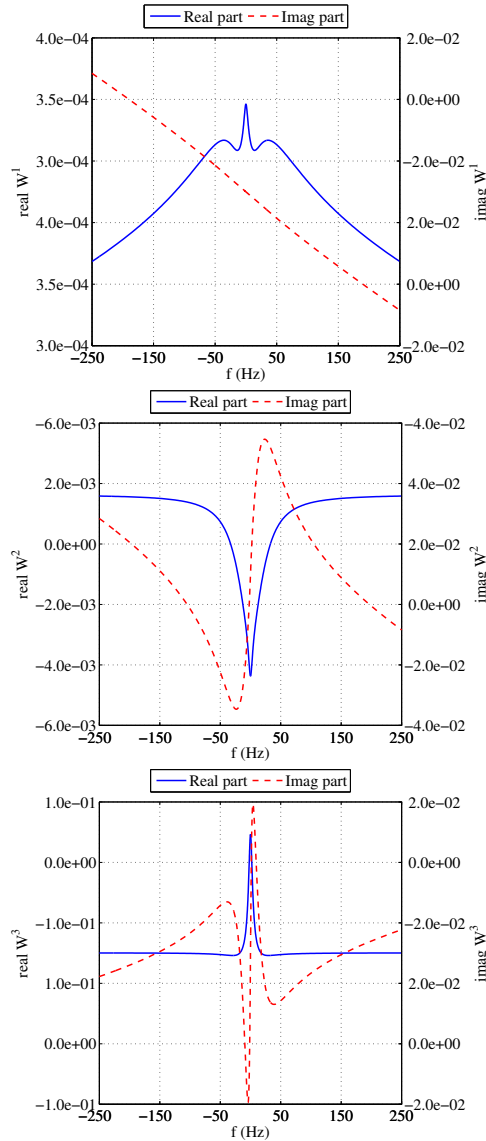
Figure 4. Single-ply composite cylinder: first 3 PGD frequency modes.

of them are complex, the real part and the imaginary part are depicted. As expected, the real part of the frequency modes is symmetric, while the imaginary part is anti-symmetric.

Notice that a uniform spatial discretization is used with 770 bilinear quadrilateral elements of size 0.01m. This implies 930 nodes with scalar complex unknowns. A non-uniform discretization is used for frequency because it varies more rapidly near the origin. The mesh consists of 500 $\mathcal{C}^0$-continuous linear elements refined around the zero-frequency using a cubic polynomial $\omega^3$ for the element length. Since frequency modes do not involve any derivative their corresponding algebraic equation can be solved point-wise. However, a FE discretization is introduced to approximate the frequency separated functions in a least-squares sense.

To further verify that the PGD approximation of the generalized transfer function $\hat{h}^n$ is reasonable, it is evaluated at the extreme frequencies 0 and 250 Hz and then compared with a direct FE resolution of (15) for those precise frequencies. Figure 5 depicts the difference between both approximations. The generalized solution gives approximations very close to those obtained with an FE computation, errors are always below $10^{-5}$.
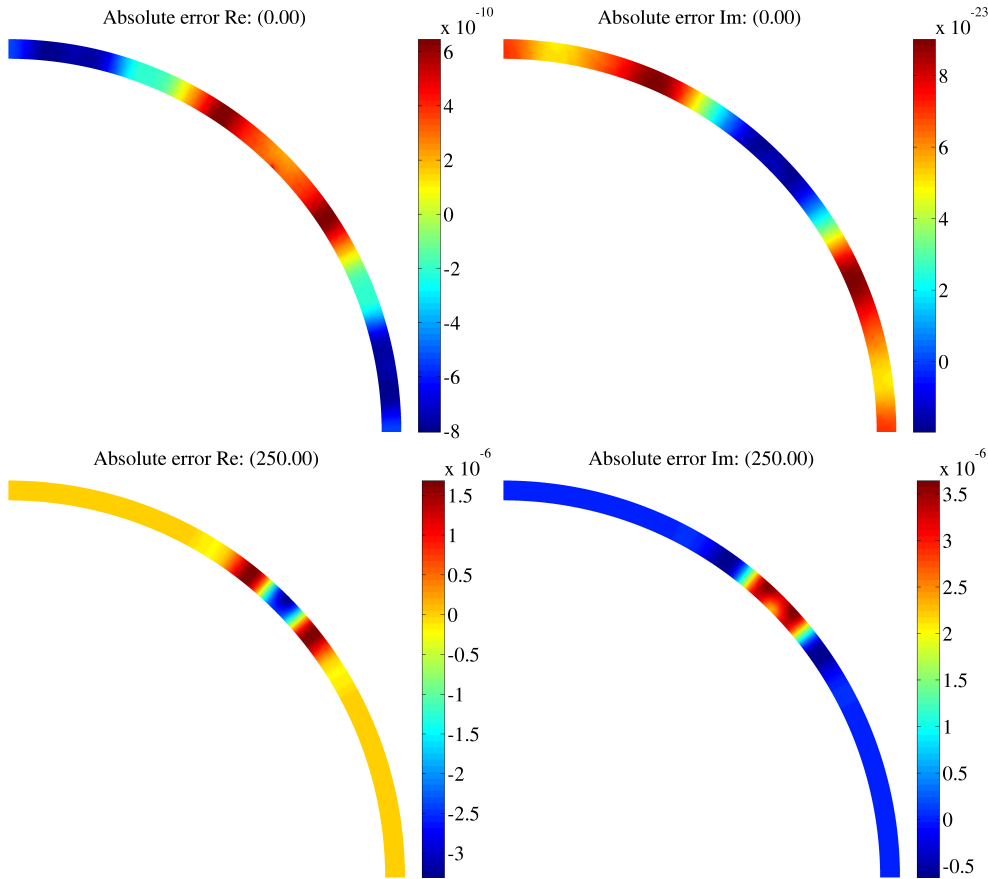
Figure 5. Single-ply composite cylinder: difference between PGD and FE solutions, real (left) and imaginary (right) parts, for frequencies 0 Hz (top) and 250 Hz (bottom).

Finally, once $\hat{h}^n$ is determined and its inverse Fourier transform computed, $h^n = \mathcal{F}^{-1}[\hat{h}^n]$, equation (18) is used to determine the temperature at the desired monitoring point $\boldsymbol{x}_0$ for a given excitation. The evaluation of the PGD approximation and its inverse Fourier transform is performed only once for any excitation, it is the offline phase. The actual application of the convolution, see equation (18), for any excitation in order to determine the temperature at the monitored point is the online or post-process phase. Here this is done for the imposed external flux $q(\xi, t)$, see equation (29), in the time interval $t \in [0, 1]$ seconds, which is the window of interest. The convolution integral is discretized in time using the time-step that comes naturally from the greatest frequency considered in the generalized transfer function. This follows the previous discussion on the use of the Nyquist-Shannon theorem [45].

The evolution with time of the temperature at $\boldsymbol{x}_0$ is shown in Figure 6. The reference solution (solid red line) is computed with FE and a Crank-Nicolson time-marching scheme. This scheme uses a ratio $\Delta t / \Delta x^2 = 20$ which has errors below $0.4\,10^{-4}$ compared with a reference solution using $\Delta t / \Delta x^2 = 1/2$ to ensure an accurate transient response. Note that each time-step requires the resolution of a system of equations whose dimension is determined by the FE mesh used.

It is clear from this figure that the proposed method produces an accurate response. However, it is more important to note that the online phase for PGD-based approximation of temperature, which is determined at 500 instants (equispaced by 2ms), requires with MATLAB® on a laptop $0.34$s, which is almost a third of the physical time 1s. This confirms that given the generalized transfer function $h^n$ and an imposed heat flux $q(\xi, t)$ along the outer boundary, the temperature at a point $\boldsymbol{x}_0$ can be evaluated in real-time (actually faster than real-time!). Note that this is 35 times faster than the full FE solution, which needs of around 12 seconds to be computed with a standard commercial code.
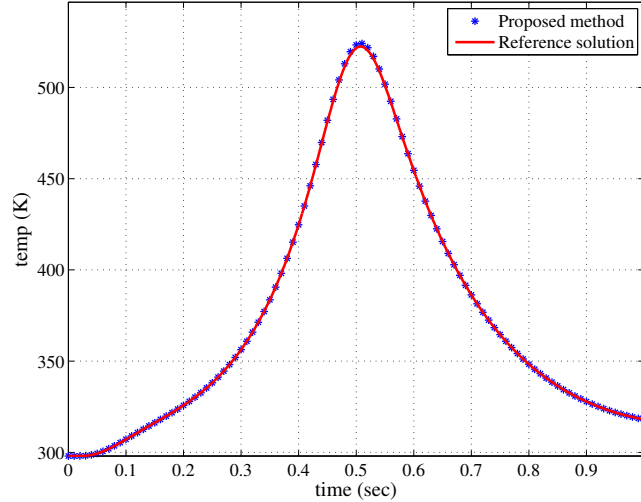
Figure 6. Single-ply composite cylinder: comparison of the temperature evolution at point $x_0$ for a moving heat flux on the outer boundary for the proposed PGD-based solution (discontinuous blue) and the standard FE (solid red).

### 5.2. *Multi-ply composite cylinder: response verification and imperfection influence*

An imperfection is introduced in the previously studied problem. That is, the same geometry, see Figure 1, and the same equations, see (28), with the same parameters are considered. However, now a zero thickness imperfection of a prescribed length is introduced in the middle of the ply just between the inner boundary and the outer boundary and centered at the measuring point. This imperfection models a possible delamination of the composite and it is modeled as a perfect adiabatic boundary. Obviously this imperfection affects convergence but not drastically, see Figure 7 for a delamination length of 0.2m. Its influence is more clear when plotting modes of the generalized transfer function. In fact, the same comparison shown earlier (that is, the difference between a PGD approximation of the generalized transfer function $\hat{h}^n$ and the direct FE) is shown in Figure 8 for the extreme frequencies 0 and 250 Hz. Recall that computations are still done for the whole range $[-250, 250]$ Hz to further verify the symmetric nature of the solution. Again errors are always below $10^{-5}$.

As discussed at the end of Section 2.3, the generalized transfer function problem (8) is non-Hermitian but it is symmetric. The later property proves sufficient for reciprocity, but it is well known that there is no proof of monotonic convergence for the PGD method when confronted to non-Hermitian operators. Thus, the convergence shown in Figure 7 shows a slight increase of the residual norm for the last computed terms.

The influence of the imperfection is even more clear when plotting temperature evolution at the measuring point. Figure 9 shows three cases with their corresponding (*expensive*) comparison with FE, the no defect case, same curves shown in Figure 6, and two defects, one of length 0.1m, the other with length 0.2m. Since the computer cost of the reference FE solution is similar to the one of the previous section, its overhead with respect to the prosed method is also of the same magnitude. The number of terms used in the PGD expansion is 21 and 25 for the short and long imperfection, respectively, recall that 19 were used with no imperfection. Thus, the imperfection does not increase the number of terms dramatically.

This methodology clearly shows that, in real-time, defects can be detected as the difference between measured and computed temperature values. Moreover, it further opens the possibility to determine the defect nature from its thermal signature.
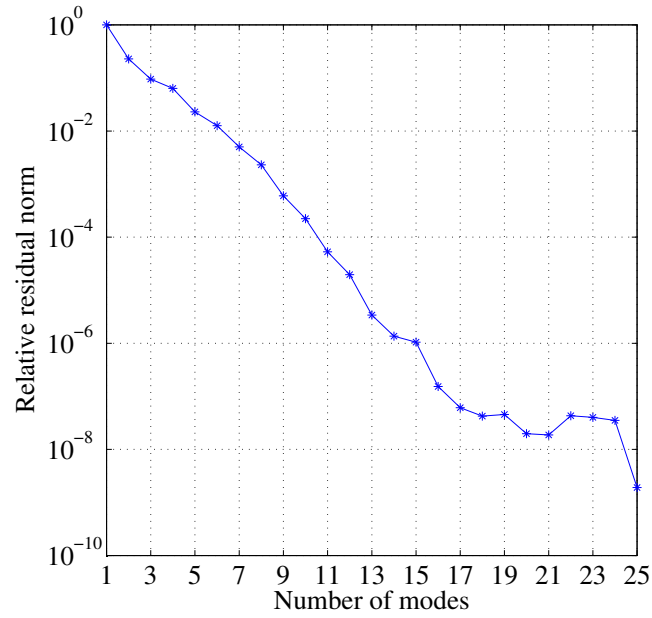
Figure 7. Multi-ply composite cylinder: convergence of the generalized frequency transfer function.
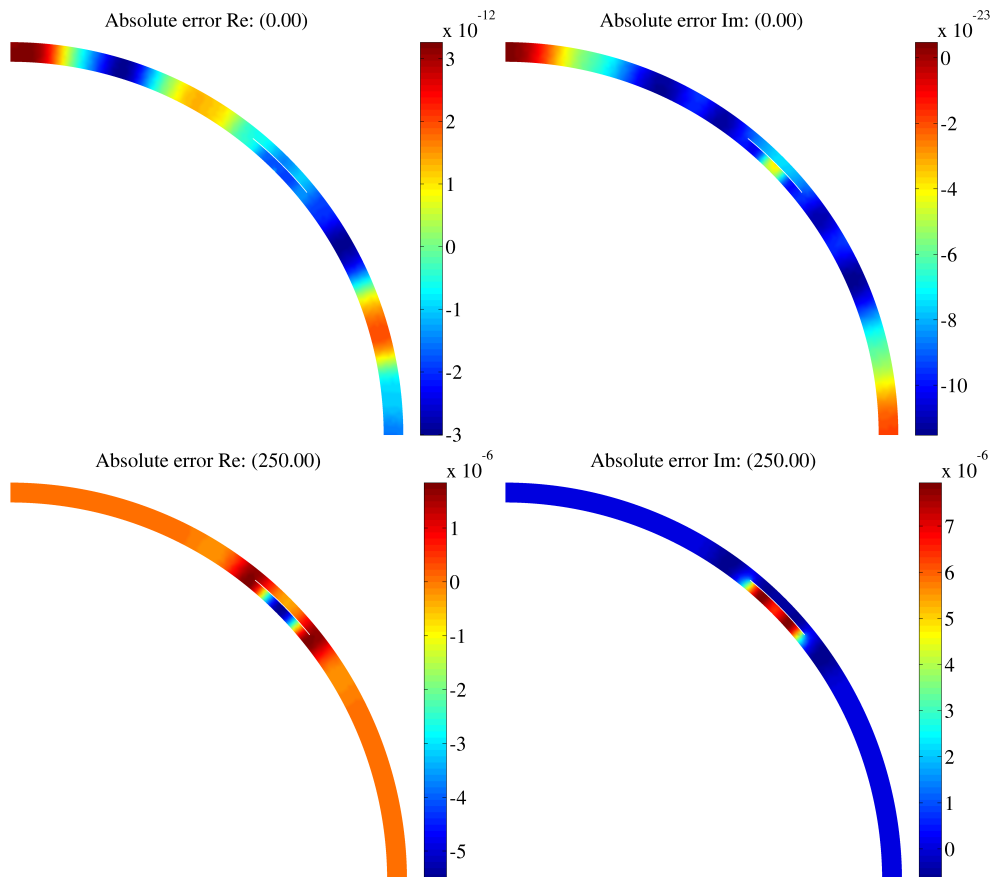


Figure 8. Multi-ply composite cylinder: difference between PGD and FE solutions, real (left) and imaginary (right) parts, for frequencies 0 Hz (top) and 250 Hz (bottom).
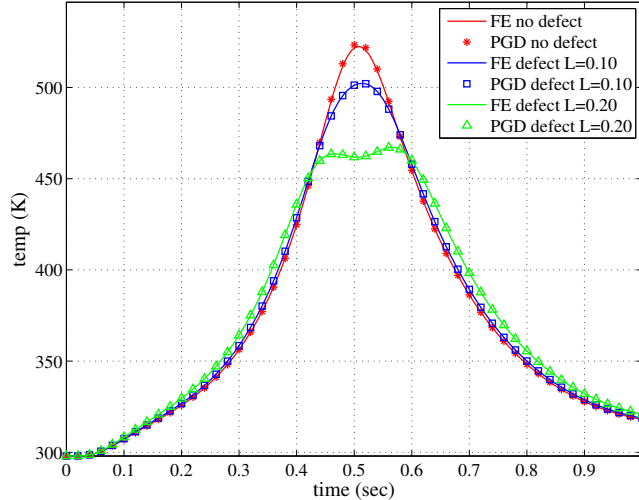
Figure 9. Multi-ply composite cylinder: comparison of the temperature evolution at point $\boldsymbol{x}_0$ for the proposed PGD-based solution (discontinuous) and the standard FE (solid) for different defect lengths.

### 5.3. Multi-parametric extension

As presented in Section 4.1 this PGD-based approach presented here has a potentiality that exceeds real-time monitoring of temperature at a given location. More precisely, thermal conductivity, $k$, can be chosen as an extra parameter. The generalized transfer function is now parametric in $k$ and consequently, temperature at the monitoring point $\boldsymbol{x}_0$ for any instance $t$ can be computed in real-time for any conductivity $k$, i.e. $u(\boldsymbol{x}_0, t, k)$, see equation (26).

The single-ply example presented and discussed in Section 5.1 is further generalized for any conductivity $k \in [1, 20]$W/(m K). In this section, the range of frequencies is up to 60 Hz instead of 250 Hz because there is no need to use the same time-step as the FE reference solution. In any case, the range of frequencies is taken such that the proper symmetries are recovered in the computed solution. This is clearly seen in the modes shown in Figures 10 and 11.

This problem however is much more challenging because there is an extra parameter. But more important, these difficulties are relevant because variations in thermal conductivity introduce major changes in the real behavior of the thermal field. This is clearly observed in the modes associated to conductivity in Figure 11. Note the large variations introduced close to the lower bound of the thermal range, recall $k \in [1, 20]$W/(m K). That is, for low conductivities solutions must localize close to the heat source. This has a clear influence in the convergence process of PGD, see Figure 12. Although convergence to engineering precision $(0.5\,10^{-2})$ is obtained with 14 modes, the rate of convergence is slower compared to space-frequency separated representations computed in the previous cases. Moreover, if further precision is required (beyond engineering accuracy), the algorithm fails to converge due to the non-Hermitian character of the operator. See [46] for further details and strategies to overcome this issue. Moreover, regarding the fixed-point convergence of the multi-parametric problem (i.e. convergence of each greedy algorithm), the average number of iterations per mode is now increased to 59. Consequently, a total of 826 FE solves are done during the offline phase to compute the necessary 14 terms of the PGD expansion. Note, that a *brute force* approach sampling (no functional approximation) of the generalized transfer function at the 121 frequency and 77 conductivity nodes would imply 9317 FE solves. The cost of the *brute force* computation of the transfer functions depends on the fidelity of the discretization of the frequency and conductivity spaces. Whereas, the cost of the computation of the PGD expansion (and the number of terms in the expansion) is largely independent of the fidelity of the discretization of the frequency and conductivity spaces, assuming the discretization is sufficiently fine.

Nevertheless, the PGD-based scheme converges globally although its local behavior, precisely for low conductivity, shows less precision compared to larger values of $k$. This is better appreciated in
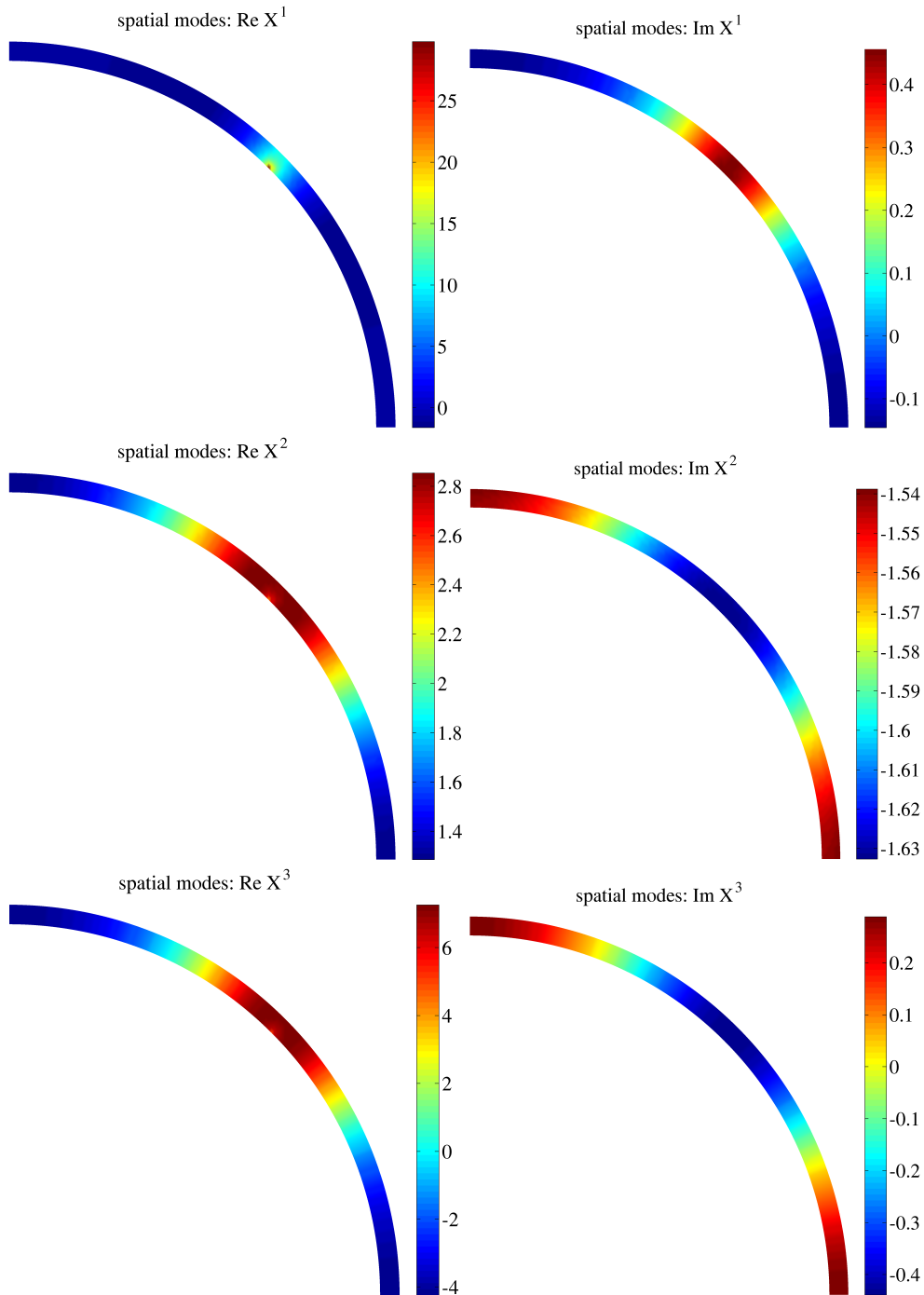
Figure 10. Single-ply multi-parametric composite cylinder: first 3 PGD spatial modes real (left) and imaginary (right).

the temperature evolution at the measuring point. Figure 13 shows this evolution for several values of the conductivity with their corresponding (*expensive*) comparison with FE. Results are in very good agreement with the reference FE solution and precision increases as $k$ increases.

Since the largest frequency considered for the evaluation of the generalized transfer function is 60Hz, the response at the measuring point $\boldsymbol{x}_0$ is recovered with a time-step of 8ms, recall (30). Consequently, the computational time needed for the online phase is faster than in previous
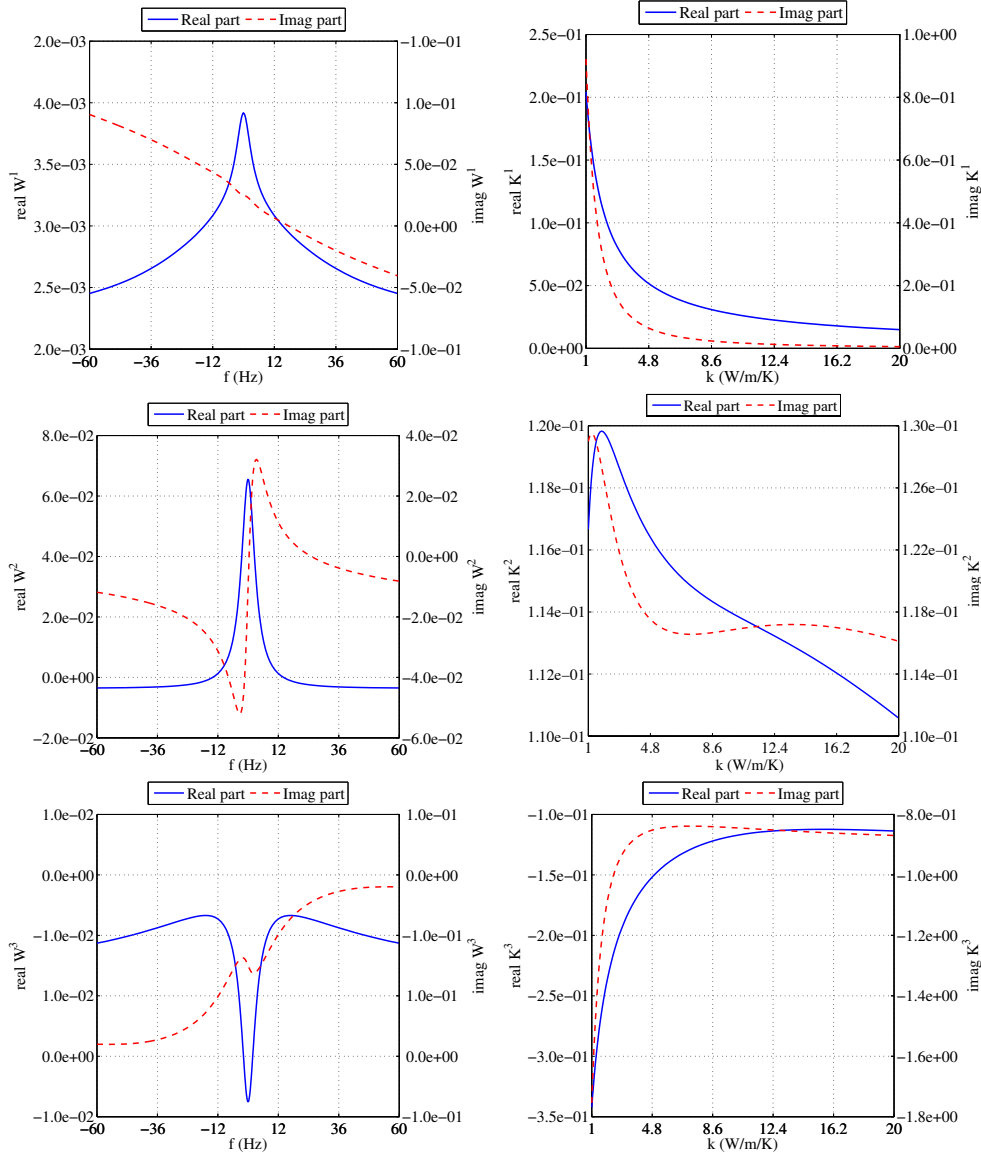
Figure 11. Single-ply multi-parametric composite cylinder: first 3 PGD frequency (left) and thermal conductivity (right) modes.

examples, only $0.09$ seconds. Whereas, the FE reference solution is computed with the same time-marching scheme described in previous sections ($\Delta t = 2$ms) because this implies that $20 \leq k\Delta t/\Delta x^2 \leq 400$. Therefore, both solutions are not strictly comparable. The computational time associated to the FE solution remains unchanged (around 12 seconds) and the online stage of the proposed approach is now 133 times faster than the FE one.

This example clearly demonstrates the applicability of this approach to inverse problems where the measured temperature can be used to determine thermal conductivity.

## 5.4. Amplitude identification

This example shows the applicability of the proposed approach for the model case of identification discussed in Section 4.2. First, some measured temperature is needed, that is, $u^{\mathrm{meas}}(\boldsymbol{x}_0, t_r)$ for $r = 1, \ldots, m$. In this case, the "measured" temperature is synthetically generated at $m = 501$ instances ($\Delta t = 2$ms) with an inflow forcing excitation equal to the one defined in (29) whose
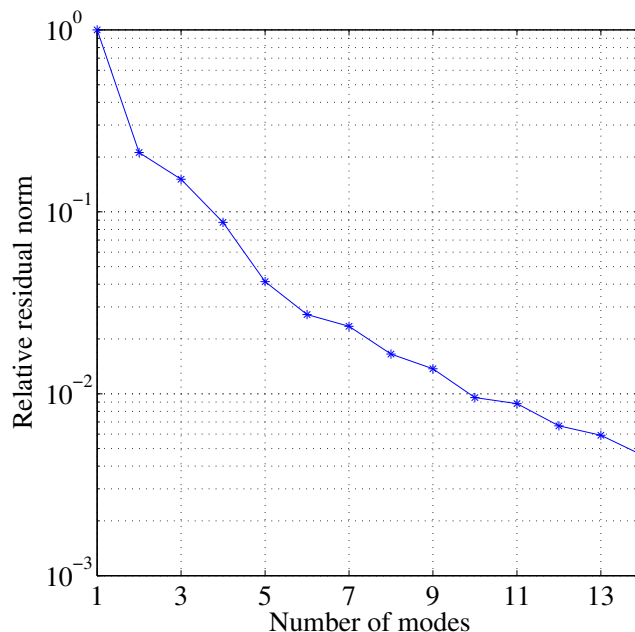
Figure 12. Multi-parametric convergence of the generalized frequency transfer function.
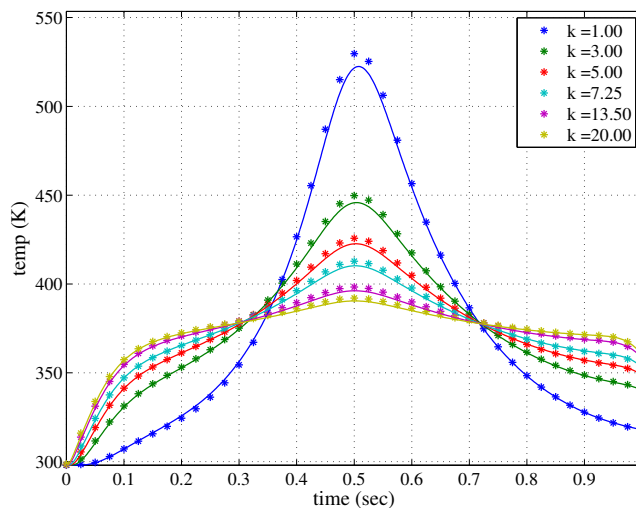


Figure 13. Multi-parametric comparison of the temperature evolution at point $x_0$ for the proposed PGD-based solution (discontinuous) and the standard FE (solid) for thermal conductivities.

amplitude is modulated by $[1 + \cos(2\pi t)]/2$. That is, a FE code with a Crank-Nicolson time-marching scheme is used to generate the temperature data at the monitoring point under an external heat source

$$q(\xi, t) = 250[1 + \cos(2\pi t)] \exp\left(-50(2\xi - \pi t)^2\right) \text{W/m}^2.$$

Second, this data is used to determine the laser input amplitude following the procedure described in Section 4.2. The amplitude of the excitation is assumed not known and it is approximated following a piecewise linear approximation with $n_{\text{fit}} = 50$ (i.e. a uniform mesh of 51 nodes each 20ms), see (27). Figure 14 shows the synthetically generated temperature at the monitoring point (left) and a comparison (right) between the approximated nodal values (blue markers) and the reference amplitude (solid red line). The coincidence is remarkable.
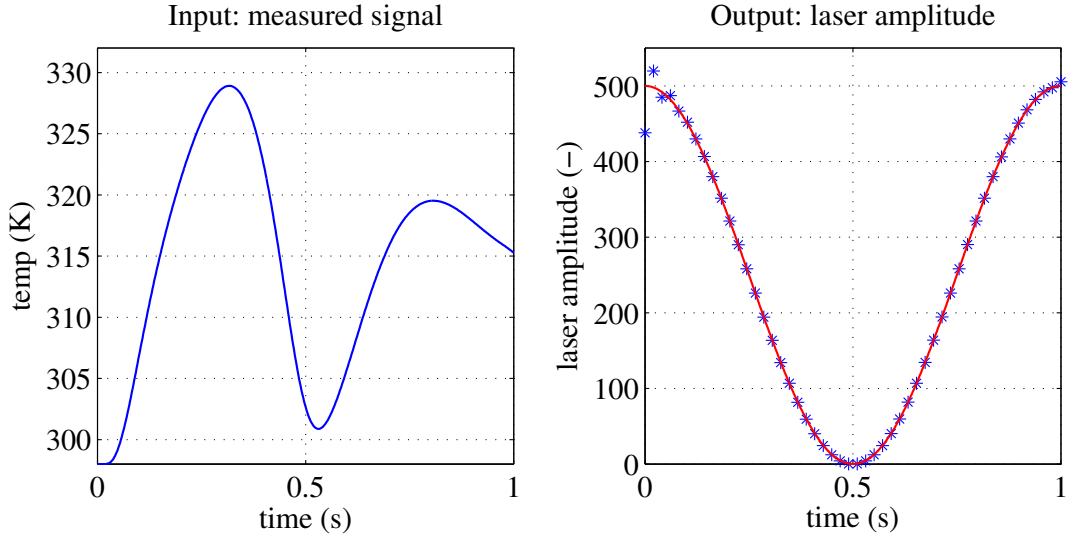
Figure 14. Amplitude identification: synthetically generated temperature measurements (left) used to calibrate the amplitude of the heat source (right), calibrated values (blue markers) and reference solution (solid red line).

## 6. CONCLUSIONS

This paper proposes a novel approach to monitor in real-time thermal processes. This technique provides temperature evolution at a particular point in the domain, usually, where thermocouples will be placed. The online computation is drastically speed-up. This can be used in a large number of problems ranging from a simple surveillance of the process to a simulation-based control, as well as identification problems for defects, material properties or power oscillations.

This approach recourses to the reciprocity principle, which can be employed in thermal problems when working in the frequency domain where the equation is symmetric (but not Hermitian). Then a convolution of the heat source and a generalized transfer function is the only computational effort that the online stage requires. Note that the generalized transfer function is determined by means of the Proper Generalized Decomposition for all the range of frequencies excited by the heat source.

Numerical results show the potentiality and the accuracy of this approach. Examples of real-time monitoring, defect detection, multi-parametric evaluation and inverse calibration are shown.

## A. GREEN'S FUNCTION PROBLEM FOR A PARABOLIC OPERATOR

Although what follows is well known it is not standard to write the Green's function problem associated to the homogenous heat equation with homogeneous Dirichlet and non-homogeneous Neumann boundary conditions. The adjoint Green's function problem associated to (2) is detailed in (3) where its last equation, namely $G = 0$ on $\Omega \times [t_0, T[$, corresponds to the *causality* condition. Green's identity can be written as

$$\int_\Omega \int_0^{t_0} \Big[ G(\nabla^2 u - \partial_t u) - u(\nabla^2 G + \partial_t G) \Big] dt d\Omega$$

$$= \int_{\partial\Omega} \int_0^{t_0} \Big[ G(\boldsymbol{n} \cdot \nabla)u - u(\boldsymbol{n} \cdot \nabla)G \Big] dt d\Gamma + \int_\Omega \Big[ uG|_{t=0} - uG|_{t=t_0} \Big] d\Omega. \quad (31)$$

Consequently, using (2) and (3) in the previous identity (31), a representation for $u(\boldsymbol{x}_0, t_0)$ with $(\boldsymbol{x}_0, t_0) \in \Gamma_N \times ]0, T[$ is obtained, namely

$$u(\boldsymbol{x}_0, t_0) = \int_{\Gamma_N} \int_0^{t_0} G(\boldsymbol{x}, t; \boldsymbol{x}_0, t_0) \, q(\boldsymbol{x}, t) dt d\Gamma + \int_\Omega u_0(\boldsymbol{x}) \, G(\boldsymbol{x}, 0; \boldsymbol{x}_0, t_0) d\Omega, \qquad (32)$$

where now it can be clearly identified that the *causality* condition implies that the solution at time $t_0$ cannot depend on any of its values at later times. Recall $T$ can be arbitrarily large.

## B.  RECIPROCITY PROOF IN THE FREQUENCY DOMAIN FOR EVEN AND ODD REAL EXCITATIONS

This appendix is aimed to prove the reciprocity principle, recall (13)

$$\langle \hat{q}_1, \hat{u}_2 \rangle = \langle \hat{q}_2, \hat{u}_1 \rangle, \qquad (33)$$

when both $\hat{q}_1$ and $\hat{q}_2$ are real. As discussed in Section 2.5, reciprocity, holds if the two conditions stated in equation (14) are verified, namely

$$\big(\nabla \hat{u}_1, \nabla \hat{u}_2\big) = \big(\nabla \hat{u}_2, \nabla \hat{u}_1\big) \text{ and } \big(\hat{u}_1, \hat{u}_2\big) = \big(\hat{u}_2, \hat{u}_1\big).$$

Recalling that $(\cdot, \cdot)$ is the $\mathcal{L}^2$ scalar product of *complex* functions in $\Omega$, see (9), these conditions are equivalent to

$$\text{Im}\Big[\big(\nabla \hat{u}_1, \nabla \hat{u}_2\big)\Big] = 0 \text{ and } \text{Im}\Big[\big(\hat{u}_1, \hat{u}_2\big)\Big] = 0.$$

Since $\hat{u}_1$ and $\hat{u}_2$ give values in $\mathbb{C}$, one can define the real functions $a_1$, $b_1$, $a_2$ and $b_2$ such that $\hat{u}_1 = a_1 + ib_1$ and $\hat{u}_2 = a_2 + ib_2$, and the previous expressions are equivalent to

$$\big(\nabla a_1, \nabla b_2\big) = \big(\nabla b_1, \nabla a_2\big) \qquad (34a)$$

$$\big(a_1, b_2\big) = \big(b_1, a_2\big). \qquad (34b)$$

Recall also that $\hat{u}_1$ and $\hat{u}_2$ are the corresponding solutions of the weak problem (8) for the two excitations $\hat{q}_1$ and $\hat{q}_2$ and for any imposed frequency $\omega$. By definition, $a_i$ and $b_i$ for $i = 1, 2$ also belong to space of trial and test functions, namely $\mathcal{H}^1_{\Gamma_D}$. Thus, equation (8) for the pair $\{\hat{u}_1, \hat{q}_1\}$ can be particularized as follows:

$$\begin{aligned}\big(\nabla \hat{u}_1, \nabla a_2\big) + i\omega \big(\hat{u}_1, a_2\big) &= \langle \hat{q}_1, a_2 \rangle, \\ \big(\nabla \hat{u}_1, \nabla b_2\big) + i\omega \big(\hat{u}_1, b_2\big) &= \langle \hat{q}_1, b_2 \rangle,\end{aligned} \qquad (35)$$

and likewise for $\{\hat{u}_2, \hat{q}_2\}$

$$\begin{aligned}\big(\nabla \hat{u}_2, \nabla a_1\big) + i\omega \big(\hat{u}_2, a_1\big) &= \langle \hat{q}_2, a_1 \rangle, \\ \big(\nabla \hat{u}_2, \nabla b_1\big) + i\omega \big(\hat{u}_2, b_1\big) &= \langle \hat{q}_2, b_1 \rangle.\end{aligned} \qquad (36)$$

Recall the splitting of $\hat{u}_1$ into real and imaginary parts, $\hat{u}_1 = a_1 + ib_1$, to also split equations (35) into real and imaginary parts as

$$\big(\nabla a_1, \nabla a_2\big) - \omega \big(b_1, a_2\big) = \langle \hat{q}_1, a_2 \rangle, \qquad (37a)$$

$$\big(\nabla b_1, \nabla a_2\big) + \omega \big(a_1, a_2\big) = 0, \qquad (37b)$$

$$\big(\nabla a_1, \nabla b_2\big) - \omega \big(b_1, b_2\big) = \langle \hat{q}_1, b_2 \rangle, \qquad (37c)$$

$$\big(\nabla b_1, \nabla b_2\big) + \omega \big(a_1, b_2\big) = 0, \qquad (37d)$$

where the hypothesis that both $\hat{q}_1(\boldsymbol{x}, \omega)$ and $\hat{q}_2(\boldsymbol{x}, \omega)$ belong to $\mathbb{R}$ is used.

Likewise, for $\hat{u}_2 = a_2 + ib_2$ each equation in (36) is split into real and imaginary parts as

$$\big(\nabla a_2, \nabla a_1\big) - \omega\big(b_2, a_1\big) = \big\langle \hat{q}_2, a_1 \big\rangle \tag{38a}$$

$$\big(\nabla b_2, \nabla a_1\big) + \omega\big(a_2, a_1\big) = 0 \tag{38b}$$

$$\big(\nabla a_2, \nabla b_1\big) - \omega\big(b_2, b_1\big) = \big\langle \hat{q}_2, b_1 \big\rangle \tag{38c}$$

$$\big(\nabla b_2, \nabla b_1\big) + \omega\big(a_2, b_1\big) = 0 \tag{38d}$$

Recall now that the $\mathcal{L}^2$ scalar product is symmetric for any pair of real functions, more specifically $(u,v) = (v,u)$ for all $u$ and $v \in \mathbb{R}$. Then subtract (38b) from (37b), and (38d) from (37d) to obtain the desired conditions (34). Thus if (34) are verified, then (14) also holds and reciprocity is demonstrated. Note that these results hold for any $\omega$.

To further close these appendix, note that the other equations not used up to now also produce the same results. After subtracting (38a) from (37a) and (38c) from (37c), the following equations are obtained:

$$\omega\Big[\big(b_2, a_1\big) - \big(b_1, a_2\big)\Big] = \big\langle \hat{q}_1, a_2 \big\rangle - \big\langle \hat{q}_2, a_1 \big\rangle,$$

$$\big(\nabla a_1, \nabla b_2\big) - \big(\nabla a_2, \nabla b_1\big) = \big\langle \hat{q}_1, b_2 \big\rangle - \big\langle \hat{q}_2, b_1 \big\rangle.$$

However, both left-hand-sides in the previous equations are zero because they correspond to (34), which was just proven, and these equations become

$$\big\langle \hat{q}_1, a_2 \big\rangle = \big\langle \hat{q}_2, a_1 \big\rangle \text{ and } \big\langle \hat{q}_1, b_2 \big\rangle = \big\langle \hat{q}_2, b_1 \big\rangle,$$

which corresponds to split (33) into real and imaginary parts using the definitions splitting of $\hat{u}_1 = a_1 + ib_1$ and $\hat{u}_2 = a_2 + ib_2$.

## REFERENCES

1. Love AEH. *A treatise on the Mathematical Theory of Elasticity*. 4th edn., Dover Publications: New York, NY, 1944.
2. Ammar A, Mokdad B, Chinesta F, Keunings R. A new family of solvers for some classes of multidimensional partial differential equations encountered in kinetic theory modeling of complex fluids. Part II: transient simulation using space-time separated representations. *J. Non-Newtonian Fluid Mech.* 2007; **144**(2-3):98–121.
3. Chinesta F, Ladevèze P, Cueto E. A short review on model order reduction based on Proper Generalized Decomposition. *Arch. Comput. Methods Eng.* 2011; **18**(4):395–404.
4. Chinesta F, Leygue A, Bordeu F, Aguado J, Cueto E, Gonzalez D, Alfaro I, Ammar A, Huerta A. PGD-based computational vademecum for efficient design, optimization and control. *Arch. Comput. Methods Eng.* 2013; **20**(1):31–59.
5. Clough RW, Penzien J. *Dynamics of Structures*. 2nd edn., Civil engineering series, McGraw-Hill: New York, NY, 1993.
6. Bathe KJ. *Finite Element Procedures*. Civil engineering series, Prentice-Hall: Englewood Cliffs, NJ, 2006.
7. Hughes TJR. *The finite element method: linear static and dynamic finite element analysis*. Dover Publications: New York, 2000. Corrected reprint of the 1987 original [Prentice Hall, Englewood Cliffs, NJ].
8. Zienkiewicz OC, Taylor RL. *The finite element method. Vol. 2 Solid mechanics*. fifth edn., Butterworth Heinemann: Oxford, 2000.
9. Ladevèze P, Arnaud L, Rouch P, Blanzé C. The variational theory of complex rays for the calculation of medium-frequency vibrations. *Eng. Comput.* 2001; **18**(1-2):193–214.
10. Rouch P, Ladevèze P. The variational theory of complex rays: A predictive tool for medium-frequency vibrations. *Comput. Meth. Appl. Mech. Eng.* 2003; **192**(28-30):3301–3315.
11. Ladevèze P, Riou H. Calculation of medium-frequency vibrations over a wide frequency range. *Comput. Methods Appl. Mech. Engrg.* 2005; **194**(27-29):3167–3191.
12. Dorival O, Rouch P, Allix O. A substructured version of the variational theory of complex rays dedicated to the calculation of assemblies with dissipative joints in the medium-frequency range. *Eng. Comput.* 2006; **23**(7-8):729–748.
13. Riou H, Ladevèze P, Sourcis B. The multiscale VTCR approach applied to acoustics problems. *J. Comput. Acoust.* 2008; **16**(4):487–505.
14. Kovalevsky L, Ladevèze P, Riou H, Bonnet M. The variational theory of complex rays for three-dimensional Helmholtz problems. *J. Comput. Acoust.* 2012; **20**(4):1250 021. URL http://dx.doi.org/10.1142/S0218396X1250021X, 25 pages.
15. Kovalevsky L, Ladevèze P, Riou H. The Fourier version of the Variational Theory of Complex Rays for medium-frequency acoustics. *Comput. Methods Appl. Mech. Eng.* 2012; **225**:142–153.

16. Rouch P, Blanzé C. Vibrational analysis of structures with stochastic interfaces in the medium-frequency range: Experimental validation on a touch screen. *J. Sound Vibr.* 2014; **333**(6):1612–1628.

17. Barbarulo A, Ladevèze P, Riou H, Kovalevsky L. Proper Generalized Decomposition applied to linear acoustic: A new tool for broad band calculation. *J. Sound Vibr.* 2014; **333**(11):2422–2431.

18. Hetmaniuk U, Tezaur R, Farhat C. Review and assessment of interpolatory model order reduction methods for frequency response structural dynamics and acoustics problems. *Internat. J. Numer. Methods Engrg.* 2012; **90**(13):1636–1662.

19. Park H, Cho D. The use of the Karhunen-Loève decomposition for the modeling of distributed parameter systems. *Chem. Eng. Sci.* 1996; **51**(1):81–98.

20. Maday Y, Ronquist EM. The reduced basis element method: application to a thermal fin problem. *SIAM J. Sci. Comput.* 2004; **26**(1):240–258.

21. Białecki R, Kassab A, Fic A. Proper orthogonal decomposition and modal analysis for acceleration of transient FEM thermal analysis. *Int. J. Numer. Methods Eng.* 2005; **62**(6):774–797.

22. Videcoq E, Quemener O, Lazard M, Neveu A. Heat source identification and on-line temperature control by a branch eigenmodes reduced model. *Int. J. Heat Mass Transfer* 2008; **51**(19-20):4743–4752.

23. Girault M, Videcoq E, Petit D. Estimation of time-varying heat sources through inversion of a low order model built with the modal identification method from in-situ temperature measurements. *Int. J. Heat Mass Transfer* 2010; **53**(1-3):206–219.

24. Ghnatios C, Masson F, Huerta A, Leygue A, Cueto E, Chinesta F. Proper Generalized Decomposition based dynamic data-driven control of thermal processes. *Comput. Methods Appl. Mech. Eng.* 2012; **213-216**:29–41.

25. Prulière E, Chinesta F, Ammar A, Leygue A, Poitou A. On the solution of the heat equation in very thin tapes. *Int. J. Therm. Sci.* 2013; **65**:148–157.

26. Chinesta F, Leygue A, Bognet B, Ghnatios C, Poulhaon F, Bordeu F, Barasinski A, Poitou A, Chatel S, Maison-Le-Poec S. First steps towards an advanced simulation of composites manufacturing by automated tape placement. *Int. J. Mater. Form.* 2014; **7**(1):81–92.

27. Pinnau R, Schulze A. Model reduction techniques for frequency averaging in radiative heat transfer. *J. Comput. Phys.* 2007; **226**(1):712–731.

28. Sierociuk D, Dzieliński A, Sarwas G, Petras I, Podlubny I, Skovranek T. Modelling heat transfer in heterogeneous media using fractional calculus. *Philos. Trans. R. Soc. A-Math. Phys. Eng. Sci.* 2013; **371**(1990):20130 037. URL http://dx.doi.org/10.1098/rsta.2012.0146, 3 pages.

29. Feng Z, Chen J, Zhang Y. Real-time solution of heat conduction in a finite slab for inverse analysis. *Int. J. Therm. Sci.* 2010; **49**(5):762–768.

30. Rylatt DI, O'Donovan TS. Time and frequency domain investigation of the heat transfer to a synthetic air jet. *Journal of Physics: Conference Series* 2012; **395**(1):012 046. URL http://dx.doi.org/10.1088/1742-6596/395/1/012046, 9 pages.

31. Monteyne G, Javed S, Vandersteen G. Heat transfer in a borehole heat exchanger: Frequency domain modeling. *Int. J. Heat Mass Transfer* 2014; **69**:129–139.

32. Arias I, Achenbach JD. Rayleigh wave correction for the BEM analysis of two-dimensional elastodynamic problems in a half-space. *Int. J. Numer. Methods Eng.* 2004; **60**(13):2131–2146.

33. Vega J, Fraile A, Alarcon E, Hermanns L. Dynamic response of underpasses for high-speed train lines. *J. Sound Vibr.* 2012; **331**(23):5125–5140.

34. Temam R. *Navier-Stokes equations. Theory and numerical analysis*, *Studies in Mathematics and its Applications*, vol. 2. Revised edn., North-Holland Publishing Co., Amsterdam-New York, 1979.

35. Parés N, Díez P, Huerta A. Bounds of functional outputs for parabolic problems. I. Exact bounds of the discontinuous Galerkin time discretization. *Comput. Methods Appl. Mech. Eng.* 2008; **197**(19-20):1641–1660.

36. Duffy DG. *Green's functions with applications*. Studies in Advanced Mathematics, Chapman & Hall/CRC: Boca Raton, FL, 2001.

37. Kammler DW. *A first course in Fourier analysis*. Second edn., Cambridge University Press: Cambridge, 2007.

38. Lee J. *A first course in combinatorial optimization*. Cambridge Texts in Applied Mathematics, Cambridge University Press: Cambridge, 2004.

39. Ammar A, Chinesta F, Diez P, Huerta A. An error estimator for separated representations of highly multidimensional models. *Comput. Methods Appl. Mech. Eng.* 2010; **199**(25-28):1872–1880.

40. Lavedèze P, Chamoin L. On the verification of model reduction methods based on the proper generalized decomposition. *Comput. Methods Appl. Mech. Eng.* 2011; **200**(23-24):2032–2047.

41. Moitinho de Almeida JP. A basis for bounding the errors of proper generalised decomposition solutions in solid mechanics. *Int. J. Numer. Methods Eng.* 2013; **94**(10):961–984.

42. Nouy A. A priori model reduction through proper generalized decomposition for solving time-dependent partial differential equations. *Comput. Methods Appl. Mech. Eng.* 2010; **199**:1603–1626.

43. Pruliere E, Chinesta F, Ammar A. On the deterministic solution of multidimensional parametric models using the Proper Generalized Decomposition. *Math. Comput. Simul.* 2010; **81**(4):791–810.

44. Ammar A, Huerta A, Chinesta F, Cueto E, Leygue A. Parametric solutions involving geometry: a step towards efficient shape optimization. *Comput. Methods Appl. Mech. Eng.* 2014; **268**:178–193.

45. Shannon CE. Communication in the presence of noise. *Proc. Institute of Radio Engineers* 1949; **18**(1):10–21. Reprint as classic paper in: *Proceedings of the IEEE*, Vol. 86, No. 2, 447–457, (Feb 1998).

46. Barbarulo A. On a PGD model order reduction technique for mid-frequency acoustic. PhD Thesis, Ecole Normale Supérieure de Cachan, France Nov 2012.